Korean J. Chem. Eng., 37(2), 189-208 (2020)
DOI: 10.1007/s11814-019-0437-1
pISSN: 0256-1115
eISSN: 1975-7220

INVITED REVIEW PAPER

Graphene-based 3D lightweight cellular structures: Synthesis and applications

Min Jun Oh* and Pil J. Yoo*,,†**

*School of Chemical Engineering, Sungkyunkwan University (SKKU), Suwon 16419, Korea
**SKKU Advanced Institute of Nanotechnology (SAINT), Sungkyunkwan University (SKKU), Suwon 16419, Korea
(*Received 4 September 2019 • accepted 21 November 2019*)

Abstract−Ultralight three-dimensional (3D) cellular architectures are both a challenge and an opportunity for those academic and industrial applications involved with high performance material design. The challenges have been accessed by employing a variety of materials. Accordingly, graphene has shown greatest potential by virtue of its unique chemical, thermal, electronic, and mechanical properties for applications ranging from structural materials to energy storage/conversion devices. In this review, we highlight recent efforts and advances made in the implementation of graphene-based 3D cellular architectures, especially focusing on the ultralight density region (<10 $mg \cdot cm^{-3}$). First, we reviewed the synthetic approaches for generating graphene-based 3D lightweight cellular structures according to the criteria of closed-cellular structures (CCSs) or open-cellular structures (OCSs) whether cell faces between constituent unit cells exist or not, respectively. These structural differences could lead to discerning physical properties, such as in mass transport across pores, heat/electron transfer through graphene framework, and various modes in mechanical deformation. We then collectively introduce recent achievements for representative applications utilizing different types of cellular structures such as flexible electronics, energy storage/conversion systems, fluid absorption, mechanical dampers, and sensors. Finally, we highlight the future perspectives of graphene-based lightweight cellular structures to surpass existing technological challenges.

Keywords: Graphene, Aerogel, Lightweight, Porous Materials, Open-cellular Structures, Closed-cellular Structures

INTRODUCTION

Graphene, well-known one-atom-thick two-dimensional (2D) monolayers composed of sp^2 bonded carbons, has attracted much attention due to its remarkable physical and chemical properties, such as lightweight, high specific surface area (SSA) (~2,630 $m^2 \cdot g^{-1}$) [1,2], outstanding thermal/electronic conductivity [3-5], a wide wavelength range of light absorption [6,7], high mechanical flexibility [8], strong mechanical strength (~1 TPa) [9], and excellent chemical stability [10]. Harnessing these outstanding physical, chemical and mechanical properties of graphene, tremendous amount of researches have been reported for not only how to synthesize and structure graphene-derivative materials [11-14], but also a wide range of applications such as for flexible electronics [15], high capacity energy storage/conversion [16-18], electrochemical catalysis [19-21], gas-separation membranes [22,23], fluid absorption/separation [24-27], mechanical/acoustic damping [28], and biomedical sensors [29-31].

In the earlier period of graphene research, authors mainly focused on elucidating physical/chemical properties of graphene (unique gapless conical band structure) within atomistic level [32]. However, with the times, several graphene-related studies have been shifted to improve physical properties for maximizing the mechanical strength, production efficiency, long-term durability/stability particularly for scalable applications. Basically, this trend has been mostly driven by the development of two representative preparation methods of graphene: (1) chemical vapor deposition (CVD) of graphene monolayer, and (2) solution-based synthetic approach of graphene oxide (GO) nanoflakes. The CVD-graphene is prepared on specifically catalyzed metallic substrates (Pt, Ni, Cu) and easily transferred onto other targeted substrates [12,33]. This technique ensures the growth of large-area graphene films with high crystalline quality and allows for precise control over the number of graphene layers. On the other hand, chemical synthesis of GO is a facile and low-cost approach treating graphite powder using harsh oxidizing solution process. The GO flakes obtained from liquid phase exfoliation of graphite oxide would generally show the O/C atomic ratio of ~0.5. Subsequently, a reducing agent (hydrazine or sodium borohydride) and thermal annealing treatment under Ar or H_2 environment would remove the oxygen moieties from GOs; then the O/C ratio of reduced graphene oxide (rGO) is decreased to 0.1-0.3 according to the degree of reduction [34]. In a combination of nano- and micro-scale architecturing method, these basic building units of graphene-related materials are assembled into complexly structured architectures with enhanced properties, which are further tunable according to the targeted demand for specific applications.

Cellular structures, which are commonly observed in nature (e.g., basic framework of cork, honeycomb, or trabecular bones) [35], are highly efficient and advanced structures capable of accommodating excessive mechanical stress while retaining lightweight characteristics. Generally, the mechanical properties of lightweight cellular structured materials are varied according to intrinsic characteristics of the selected material, relative density, cell geometry, pore size, and cell size. Gibson and Ashby first derived the scaling relationship between the normalized mechanical properties of cel-

†To whom correspondence should be addressed.
E-mail: pjyoo@skku.edu

lular structure and its relative density [35].

$$\frac{\text{Mechanical property of the cellular structure } (E^* \text{ or } \sigma^*)}{\text{Mechanical property of the bulk solid material } (E_s \text{ or } \sigma_s)} = C\left(\frac{\rho^*}{\rho_s}\right)^n \quad (1)$$

where ρ^* and ρ_s are the densities of the cellular structured material and the bulk solid material, respectively, and C is a constant determined by the cell geometry. The value of n is the scaling exponent that represents the deformation mode of the cellular material, such as bending, stretching, and/or buckling. In the case of OCSs, the scaling law is written as $E^*/E_s \sim (\rho^*/\rho_s)^2$, $\sigma^*/\sigma_s \sim (\rho^*/\rho_s)^{1.5}$. For the case of ideal CCSs with a low density, the normalized mechanical properties would follow a linear scaling relationship with respect to their relative density ($E^*/E_s \sim (\rho^*/\rho_s)$, $\sigma^*/\sigma_s \sim (\rho^*/\rho_s)$). Likewise, cellular structures are commonly observed in natural materials due to their strong and stiff mechanical properties. For instance, the trabecular bone with a light density of ~0.2 g·cm^{-3} can exhibit relatively high Young's modulus of 12-120 MPa and elastic strength of ~1.36 MPa [36]. Thanks to this notable advantage, cellular structures generally offer an optimized design strategy even with sophisticated constraints in material selection. In addition, they can impart highly enlarged surface area, which is a prerequisite for the efficient mass exchange and interfacial contact between heterogeneous species. Motivated by these superior advantages in cellular structures, therefore, tremendous studies have been devoted for developing advanced lightweight cellular structures while exploiting nanocarbon-related materials (carbon nanotubes or graphene) as well as conventional ones (nanofibrous polymers or cellulosic materials). Similarly, 2D nanosheets (hexagonal boron nitride (h-BN), MoS_2, etc.) have also been utilized for structuring 3D cellular materials recently. However, considering intrinsic physical properties of the material and potential feasibility toward mass production, graphene is to be chosen as the most promising material that outperforms other candidates in realizing high performance 3D cellular structures.

In this review, we focus on the recent efforts and significant advances made in the implementation of graphene-based 3D cellular architectures within the ultralight density region (<10 mg·cm^{-3}) [37]. In particular, the ultralight density characteristic is targeted for next generation energy storage/conversion, fluid absorbing, electrical, thermal, and structural-reinforcement applications. We systematically reviewed various synthetic approaches for different types of graphene-based 3D lightweight cellular structures on the basis of structural criteria of OCSs or CCSs: whether the pore interconnectivity between neighbored cellular domains is retained or not. Subsequently, various types of cellular structures are implemented with different structural factors in the size or the shape of unit cell. These differences are directly correlated to the structural characteristics and the tunability of 3D-structured graphene monolith, especially for Young's modulus, mechanical stability, electrical conductivity, effective surface area, volumetric porosity, and transport properties. Furthermore, 3D structuring strategies are employed for synergistically combining these properties, such as using freeze-drying, hydrothermal, template-directed CVD, and 3D-printing method. Therefore, developing methods for realizing advanced 3D cellular structures of graphene with a structural hierarchy would significantly improve these material properties. As for graphene-based 3D cellular structures, they not only inherit a structural hierarchy with superior physicochemical properties, but also serve as a platform for creating novel functionalities, enabling them to be useful for diverse applications. In the following second section, we introduce recently developed strategies for utilizing the graphene-based 3D lightweight cellular structures as state-of-the-art applications for energy storage/conversion systems, electrochemical catalysts, nanoelectronics, fluid absorbers, thermal management, and mechanical dampers.

SYNTHETIC METHODS FOR GRAPHENE-BASED 3D LIGHTWEIGHT CELLULAR STRUCTURES

In the first section, we highlight the fabrication methods of graphene-based 3D lightweight cellular structures and categorize them into two groups based on the structural interconnectivity of internal pores. In general, OCSs of graphene-based 3D lightweight materials are more likely obtained from various synthetic methods, including direct gelation method of GO, self-assembly of GO followed by reduction treatment, or bottom-up growth of CVD graphene over 3D porous template of metal catalyst. On the other hand, for fabricating CCSs using GO-based materials, a water-immiscible oil phase as the counterpart of aqueous dispersion of GO is generally required. The water-immiscible oil phase is essential for the formation oil-in-water emulsions. Finally, the inner oil phase is removed and becomes empty, and the outer encompassing aqueous phase comprising GO dispersion forms cell struts and faces between individual unit cells. OCSs have well-connected internal pathways; thus, this structural characteristic would be highly beneficial for the applications requiring facilitated mass transport, such as for electrolyte-incorporated energy storage/conversion systems or fluid absorbing materials. On the other hand, CCSs with isolated unit cells would rather show some advantages in applications where the structural reinforcement is of importance. Accordingly, a fully interconnected framework including isolated internal domains would offer the maximized mechanical stability and highly enhanced thermal/electrical conductivities. In the following subsections, we introduce various preparation methods for generating graphene-based 3D lightweight cellular structures and discuss the differences in structural properties.

1. OCS: Freeze-drying Process

Freeze-drying is a conventional technique for removing liquid fraction from liquid-laden materials. From the 1990s, this technique has been widely adopted for fabricating aerogel from a gel phase while imparting material properties of flexibility, lightweight, and high strength [38,39]. In the case of applying to GO solution, a removal process of residual moisture should be essentially performed to form the porous cellular structures of graphene. This is due to the intrinsic properties of waterborne-based dispersity of exfoliated GO nanosheets. In addition, it is possible to create anisotropically aligned macroporous structures when the direction of a cold source for the freeze-drying process is controlled. This is generally termed as ice-templated unidirectional freeze casting. During the freezing step, dispersed GO nanosheets are gradually accumulated between

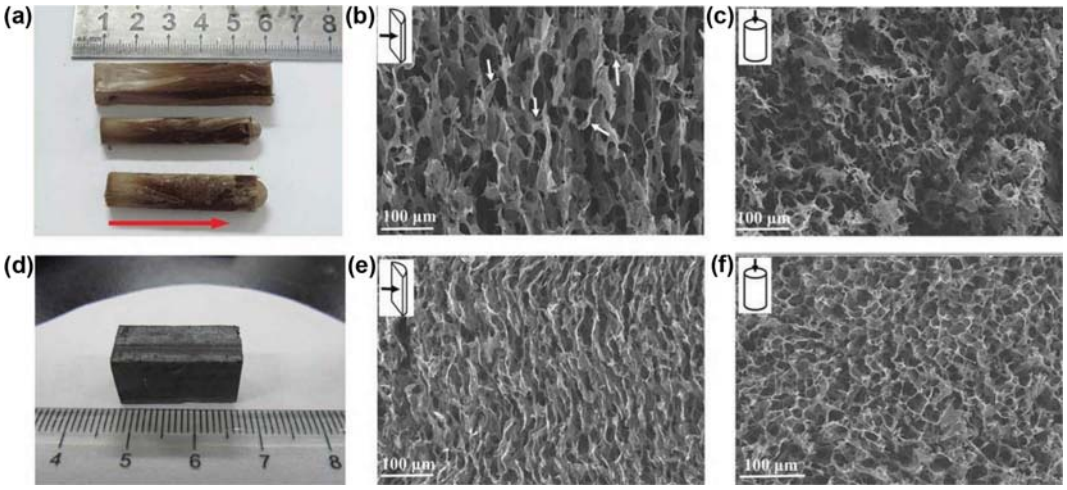

Fig. 1. (a) Digital photographic image of the GO foams. The red arrow indicates the direction of ice freezing. (b) Scanning electron microscopic (SEM) images showing longitudinal (parallel to ice freezing direction) and (c) cross-sectional (perpendicular to ice freezing direction) morphology of the as-prepared GO foam. (d) The digital image of the rGO foam. Internal microstructures of the rGO foams along the longitudinal direction (e) and cross-sectional direction (f). Reproduced with permission from ref. [40]. Copyright 2013, The Royal Society of Chemistry.

the growing ice crystals. Finally, the segregated GO layers can form the solidified columnar or lamellar-like cellular structures after the sublimation process of the ice (Fig. 1) [40].

However, 3D graphene monoliths prepared only by using freeze drying method from aqueous GO solution generally suffer from weak mechanical properties. This is because the binding interactions of van der Waals attraction between GO nanosheets are not strong enough for accommodating the externally applied stress. Therefore, to form mechanically reinforced 3D graphene aerogels (GA), some studies have introduced additional chemical bonding between GO nanosheets using thermal/chemical reduction or hybridization with other sturdy species for further imparting stronger binding interactions. For example, Sun et al. reported multifunctional ultra-flyweight ($\rho \geq 0.16\ mg \cdot cm^{-3}$) carbon aerogel, which was created by hybridizing graphene with carbon nanotubes, followed by additional chemical reduction using hydrazine vapor [41].

2. OCS: Hydrothermal Process

The hydrothermal process has been traditionally employed for a facile transformation from carbohydrate molecules to homogeneous carbon nanoparticles. Likewise, the hydrothermal process on GO aqueous solution has also been widely utilized after the first report by Zhou et al. for forming 3D graphene hydrogels [42]. This technological expansion originates from several notable advantages of the hydrothermal approach compared to conventional chemical reduction methods: (1) it only requires a simple and straightforward experimental setup of the autoclave, (2) it readily allows for production-level scalability, (3) it efficiently excludes the contamination issue from external impurities since it only uses pure water as the solvent, (4) it facilitates the structural recovery of sp^2 conjugation after the dehydration under high temperature and pressure condition within the closed autoclave cell, and (5) it offers easy controllability over the degree of reduction simply by varying the parameters of temperature or pressure. First, Zhou et al. reported hydrothermal dehydration method for a green reduction of exfoliated GOs to graphene [42]. They carefully controlled the reduction temperature and analyzed the corresponding mechanical characteristics of rGOs. Motivated by this pioneering approach, Xu et al. reported a formation of self-assembled 3D graphene hydrogels using the hydrothermal process (Fig. 2(a)) [43]. They identified that the graphene hydrogel formation was feasible only within a specific concentration range ($>1\ mg \cdot cm^{-3}$). Also, they analyzed the mechanical and electrical properties of resulting graphene hydrogels according to the variation of thermal reduction time performed at 180 °C (Fig. 2).

By virtue of the development of this facile and controllable method, numerous studies for generating graphene hydrogels or aerogels have been reported. Among them, Wu et al. reported 3D graphene spongy-like structure which possessed super-compressive elasticity and near-zero Poisson ratio characteristics [44]. Meanwhile, they also referred to the limitation of freeze-drying process [45], mostly originating from the structural asymmetry by the directional ice removal during the sublimation process. Hence, they proposed an advanced approach to minimize the structural asymmetry of hydrogels while retaining super-elasticity (recover up to 98% compression in air) and lightweight properties (0.3 to 14 $mg \cdot cm^{-3}$) by employing ethanol-solvent-based anisotropic solvothermal process. The required amount of GO (having ~20 to 50 μm in lateral sizes) solution for forming the cellular structures could be substantially reduced to half that required for the case of using pure aqueous solvent [44]. In a similar way to freeze-drying, additional reducing or cross-linking methods have also been introduced for imparting stronger cohesive interactions or forming the covalent bonding between rGO nanosheets. In due course, the hydrothermal process has become one of the most widely accepted procedures for the hydrogelation of GO solution.

3. OCS: Chemical Reducing or Cross-linking Process

As introduced in the preceding regarding freeze-drying and hydrothermal processes, researchers have attempted to create aero-

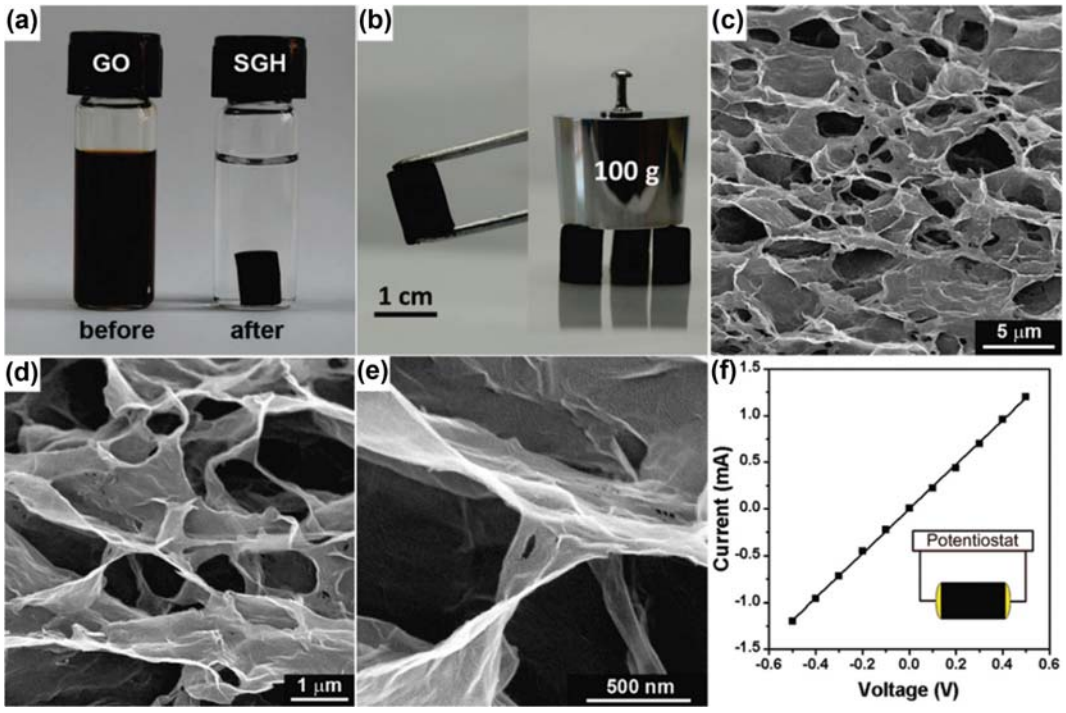

Fig. 2. (a) Digital photographic images of homogeneous GO aqueous dispersion (2 mg·ml^{-1}) before and after hydrothermal reduction at 180 °C for 12 h. (b) Photographs of strongly self-assembled graphene hydrogels allowing easy handling and supporting weight. (c)-(e) SEM images of interior microstructures with different magnifications for self-assembled graphene hydrogels. (f) Room temperature I-V curve of the self-assembled graphene hydrogel exhibiting Ohmic characteristic. Reproduced with permission from ref. [43]. Copyright 2010, American Chemical Society.

gel-like structure using graphene nanosheets while simultaneously imparting lightweight and high mechanical strength properties. To attain this goal, further reducing or cross-linking process has been generally introduced to strengthen the interconnectivity between building units of graphene. Therefore, higher degree of reduction could secure a greater amount of recovery of the sp^2 conjugation that manifests not only the formation of stronger interactions between basal planes of rGO nanosheets but also the reinforced mechanical strength of the GA structures [46]. For instance, Chen et al. reported chemically reduced lightweight GAs with a density of ~15 mg·cm^{-3} using a freeze-drying of GO with a mild reducing agent, such as vitamin C, Na_2S, HI, and $NaHSO_3$ [47]. Similarly,

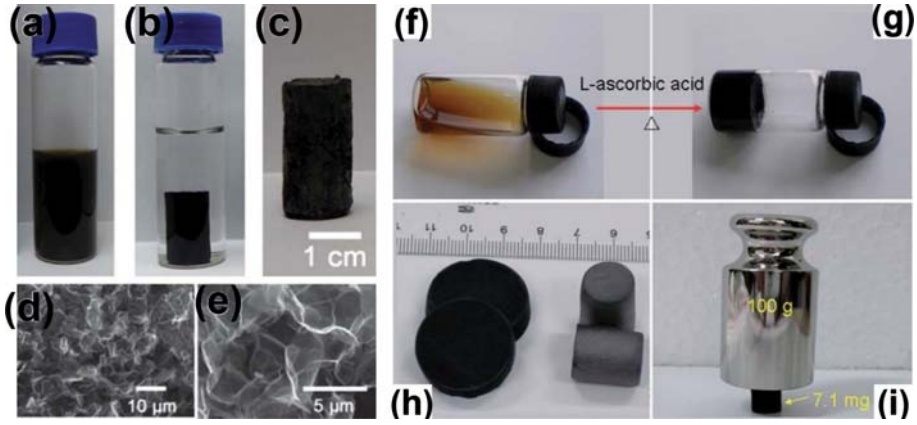

Fig. 3. (a) Digital photographic images of aqueous suspension of GO with oxalic acid and NaI before the reaction, (b) graphene hydrogel after the reduction reaction, and (c) freeze-dried aerogel. (d) and (e) SEM images of the freeze-dried GA with different magnifications. Digital images of aqueous suspension of GO (f) and graphene hydrogel stored in a vial prepared by heating the mixture of GO and L-ascorbic acid without stirring (g). (h) GAs with supercritical CO_2-drying (left) and freeze-drying (right). (i) 7.1 mg-weigh-GA pillar supporting a 100 g counterpoise. Reproduced with permission from ref. [48]. Copyright 2012, The Royal Society of Chemistry. Reproduced with permission from ref. [49]. Copyright 2011, The Royal Society of Chemistry.

Zhang et al. reported a chemical reduction-induced preparation of lightweight GAs with the density range from 2.2 to 14.2 mg·cm^{-3} by using the combination of oxalic acid and NaI species (Fig. 3(a)-(e)) [48]. In addition, other reducing agents, such as ascorbic acid (Fig. 3(f)-(i)) [45,49,50], ammonia [24,51], ethylenediamine [52], and mixture of H_3PO_2 and I_2, have also been suggested for inducing the higher-degree reduction of GO solution to compensate for the limitation of the conventional freeze-drying process [53].

However, the establishment of superelastic and highly flexible 3D-structured GAs has confronted a great challenge due to the problems of re-stacking of graphene layers, structural collapse, and the occurrence of irreversible plastic deformation. To overcome these limitations, significant efforts have been made for attaining the enhanced mechanical durability and structural efficiency while incorporating other additive species. Zhao et al. demonstrated the nitrogen (N)-doped graphene foam with ultralow density of 2.1 mg·cm^{-3} [54]. They prepared N-doped graphene foams by means of hydrothermal assembling of GO aqueous solution in the presence of 5 vol% pyrrole, which was then freeze-dried and annealed at 1,050 °C for 3 h. The pyrrole species served not only as a nitrogen donor but also as an inter-layer swelling agent. It easily adhered to the surfaces of GO nanosheets because of the formation of pi-pi interactions or hydrogen bonding by its conjugated structure with electron-rich N atoms. Additionally, the pyrrole could substantially inhibit irreversible self-stacking between GO nanosheets during the hydrothermal reduction process, thereby facilitating the formation of GAs with a high structural efficiency. The resulting structures exhibited a high SSA of 280 m^2·g^{-1} with a predominant macroporous structure and could recover the structural volume even after applying a compressive strain of up to 60%.

In addition, Hong et al. reported polymeric cross-linked GAs using poly(vinyl alcohol) (PVA) and glutaraldehyde as the cross-linker to covalently bind each graphene nanosheet by esterification and acetalization reactions (Fig. 4) [16]. The resulting graphene/PVA monolith showed characteristics of a low density (10.6 mg·cm^{-3}), enhanced compressive modulus by a factor of 1.8 (from 91.4 to 168.6 kPa), and 8.6-times greater compressive stress (from 21.0 to 182.0 kPa) as compared to those of non-cross-linked rGO aerogels. Similarly, Qin et al. showed that superelastic graphene/polyimide (PI) aerogel could be synthesized by a co-polymerization of GO with poly(amic acid) (as a PI precursor) followed by a freeze-drying. The resulting GO/PI aerogels could exhibit robust Young's modulus

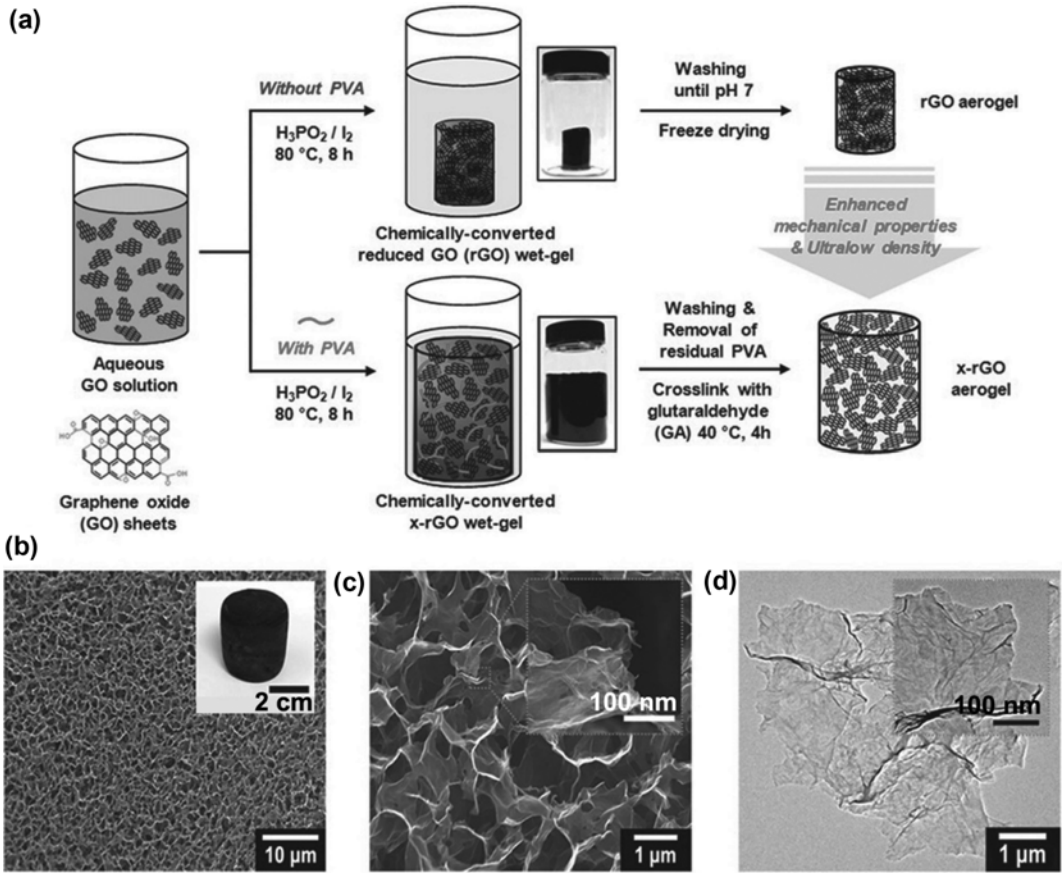

Fig. 4. (a) Schematic illustration showing different steps for selectively fabricating rGO aerogel (upper) and cross-linked rGO aerogel (lower). Insets at center show the as-prepared chemically converted rGO wet-gel (upper) and cross-linked rGO wet-gel (lower) after self-assembly. These wet-gels are transformed into graphene-based aerogels by freeze-drying method. (b) SEM image of the resulting cross-linked rGO aerogel with lower magnification. Inset shows a centimeter-sized cross-linked rGO aerogel. (c) SEM image of the cross-linked rGO aerogel. (d) Transmission electron microscopy (TEM) image of cross-linked rGO aerogel. Reproduced with permission from ref. [16]. Copyright 2015, Wiley-VCH.

property of 1.74 MPa, and its maximum yield strength value was measured to be 157.3 kPa with a lightweight density of 10 mg·cm^{-3}. Furthermore, Vinod et al. reported that GO/h-BN nanocomposite foams with a density of 5 mg·cm^{-3} could be fabricated by chemical reduction and freeze-drying using a mixed solution of GO and h-BN nanosheets [55]. The multilayered stacking/incorporation of h-BN could lead to enhanced mechanical and thermal stability, and the crack propagations were mitigated compared to the conventional GAs without h-BN.

4. OCS: Sol-gel Process

Sol-gel method, which is another efficient way to fabricate graphene-based porous structures, is a kind of polymerization process widely utilized to synthesize several mesoporous structures [56]. Importantly, sol-gel method can create foam structures by directly facilitating the formation of covalent bonds between GO nanosheets in the synthetic procedure, whereas the previously introduced methods partially utilized the implementation of additional pi-pi interactions or covalent bonds to reinforce the structural stability. First, Worsely et al. reported the synthesis of GAs using sol-gel polymerization of resorcinol (R) and formaldehyde (F) with sodium carbonate as a catalyst in a GO aqueous solution (Fig. 5) [57,58]. The resulting graphene/carbon hybridized aerogels showed a low density from ~10 mg·cm^{-3} and high SSA with 1,200 m^2·g^{-1}. The bulk properties of the resulting graphene-based aerogels, such as surface area, pore volume, pore size, and the nature of chemical bonding in carbon phase (sp^2 vs sp^3), could readily be controlled by adjusting the content of sol-gel precursor. Furthermore, Meng et al. demonstrated a graphene/carbon aerogel while excluding the use of additional catalyst during sol-gel process. They suggested the use of alkali-treated GO as a solid base catalyst to trigger the polymerization reaction of R with F [59]. The resulting graphene/carbon aerogel showed a narrow pore distribution (10-50 nm), a relatively higher density (0.11-0.19 g·cm^{-3}) and smaller SSA (361-763 m^2·g^{-1}).

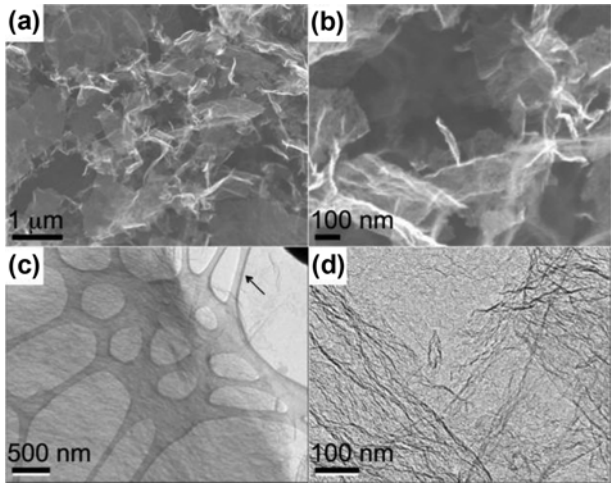

Fig. 5. Field-emission scanning electron microscopic (FE-SEM) images of the GAs with lower (a) and higher (b) magnification. TEM of the GAs with lower (c) and higher (d) magnification. Reproduced with permission from ref. [57]. Copyright 2010, American Chemical Society.

5. OCS: Template-direct CVD Process

Unlike the previously introduced self-assembly approaches using GO nanosheets as a building unit, the template-directed CVD technique could offer the merit of easily adjusting the structural factors of the resulting graphene foam [60]. To realize the feasibility of this process, in particular, the role of templating substrate is decisive and it needs to satisfy some conditions: (1) easy controllability in

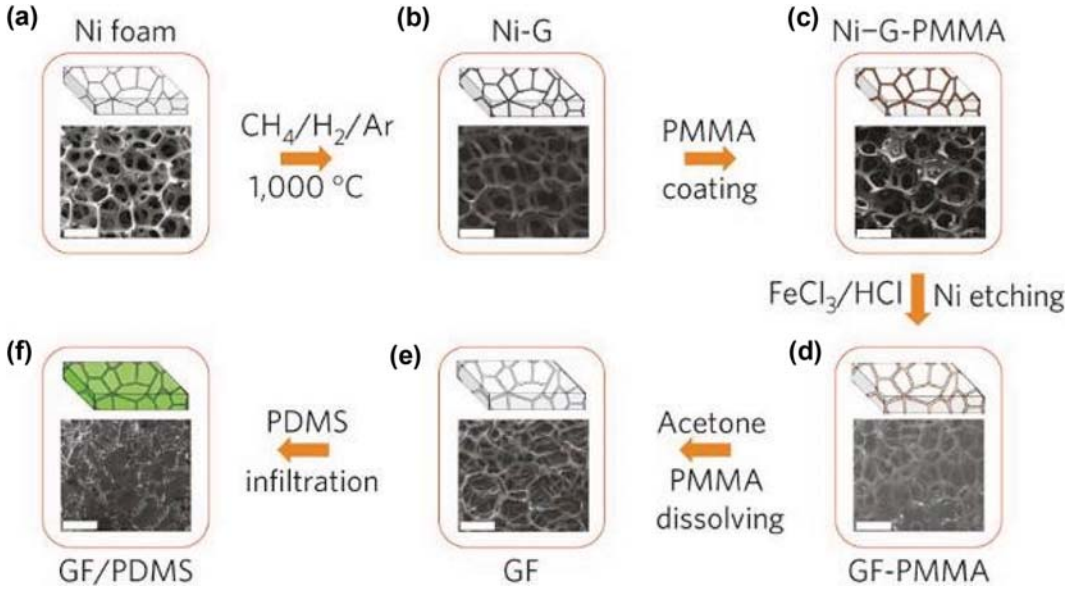

Fig. 6. Schematic procedure for fabricating graphene foam (GF)/PDMS composites. (a), (b) CVD growth of graphene films (Ni-G, b) over a nickel foam template (Ni foam, a). (c) Coating of thin poly(methyl methacrylate) (PMMA) layer over as-grown graphene film (Ni-G-PMMA). (d) GF coated with PMMA (GF-PMMA) after etching the nickel foam with hot HCl (or $FeCl_3$/HCl) solution. (e) Free-standing GF after dissolving the PMMA layer with acetone. (f) GF/PDMS composite film after infiltrating PDMS into GF. In insets of SEM images, all the scale bars are 500 μm. Reproduced with permission from ref. [8]. Copyright 2011, Nature Publishing Group.

the size and shape, (2) intrinsically OCS to facilitate the transport of gas-phase precursor, and (3) high etching selectivity without disturbing the deposited graphene layer. For these reasons, the fabricated graphene foams from templated CVD method strongly depend on the selection of the sacrificial template.

For example, Chen et al. reported flexible and conductive graphene foam on a nickel foam with an ultralow density of 5 mg·cm^{-3} (Fig. 6) using CVD method [8]. It also has a high porosity (~99.7%) and SSA up to 850 m^2·g^{-1} with an average number of deposited graphene layers of ~3. To obtain much lighter structures, Mecklenburg et al. demonstrated one of the lightest, yet mechanically robust carbon aerogels called aerographite [61]. They utilized freely adjustable 3D network of tetrapod-like ZnO as the sacrificial template. The density of resulting aerographite was only 0.18 mg·cm^{-3} by virtue of employing a novel single-step CVD method over the hierarchically interconnected ZnO tetrapod networks. Also, its Young's moduli were measured to be 15 and 0.88 kPa as tensile and compressive modulus, respectively. Furthermore, motivated by mechanically robust carbon nanotube structures, Bi et al. fabricated tubular-networked graphene cellular structures [62]. Initially, they synthesized mesoporous SiO_2 monoliths using sol-gel method as the sacrificial template, and then used template-directed CVD technique and annealed subsequently for tubular-networked GA. The resulting tubular-networked graphene cellular structures showed ultralow density (1.6 mg·cm^{-3}), excellent strength and stiffness ($E \sim \rho^{1.81}$ in the density range of 1-100 mg·cm^{-3}), full shape recovery (after 95% compression), and mechanical stability (over 80% maximum stress retention after 1,000 cycles of 80-90% compression).

6. OCS: 3D-printing Process

3D-printing has attracted great attention because it can readily and quickly create desired 3D structures with variety in material selection. For the purpose of implementing ultralight 3D-printed structures, there has also been an attempt to combine the excellent characteristics of graphene material with 3D-printing technique. For instance, García-Tuñon et al. suggested that GA could be prepared by 3D-printing in a desired way [63]. They printed the solution consisting of chemically functionalized GO nanosheets and pH-responsive polymer, which formed a stable 3D network via hydrogen bonds and hydrophobic interactions. After the subsequent freeze-drying and thermal reduction process, it underwent a transformation into lightweight structure. The resulting 3D printed structure showed a Young's modulus of 130 kPa at a density of 6 mg·cm^{-3}. However, there is still a possibility of improvement in terms of elasticity because it exhibited insufficient elasticity that could recover the deformation (up to 90%) only upon applying 20% compression.

To overcome this limitation, several strategies have been suggested to minimize the density of 3D structures and to ensure the elasticity [64-67]. For example, Zhu et al. reported highly compressible 3D GA microlattices using sol-gel precursors (R and F) to impart a proper distance between GO nanosheets and to bridge them with covalent bonds (Fig. 7) [64]. This method turned out to be effective in improving elasticity characteristics. However, the minimum density value increased to ~30 mg·cm^{-3} due to a decrease in the pore size. In addition, some approaches have been made to improve the mechanical properties by printing the mixed solution of GO and CNT [65], or direct printing of GO solution with subsequent freeze-casting [66,67].

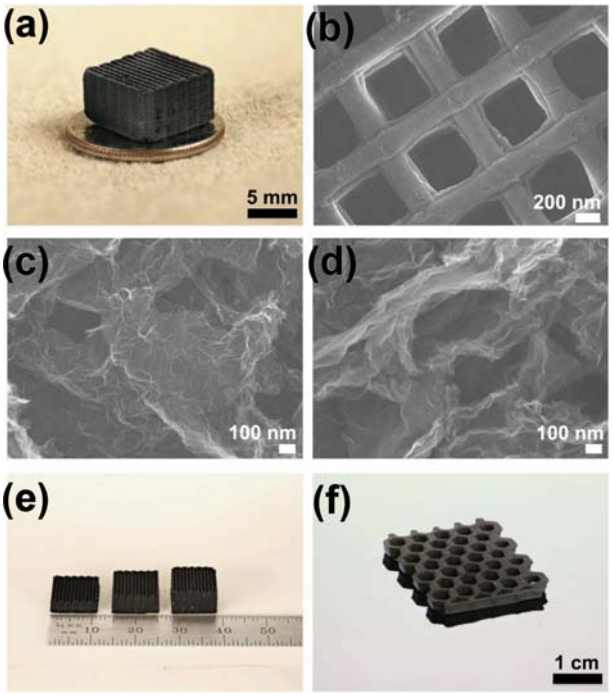

Fig. 7. (a) Digital photographic image of 3D printed GA microlattice. SEM images of (b) 3D printed GA microlattice, (c) GA without R-F after etching, and (d) GA with 4 wt% R-F after etching. Digital image of (e) 3D printed GA microlattices with varying thicknesses and (f) 3D printed GA honeycomb. Reproduced with permission from ref. [64]. Copyright 2015, Nature Publishing Group.

7. CCS: Emulsified Hydrothermal or Freeze-drying Method

It is necessary to use two immiscible phases in the synthetic process to structurally distinguish the internal void and the outer surrounding septum phases, respectively. For example, GO, most widely used structuring material, can easily be prepared as a dispersed state in water. Therefore, one feasible way to fabricate a CCS using water-soluble GO would be to create the oil-in-water emulsion by introducing water-immiscible organic phase. Particularly, dispersed GO has the characteristic of assembling at the interface with immiscible phase, much like as a surfactant molecule, which allows for the emulsion interface to be considerably stable without causing problematic cases of merging or collapse [68-70]. Li et al. proposed closed-cellular macroporous graphene monoliths prepared from oil (hexane)-in-water (GO solution) emulsified hydrothermal method. The resulting hydrogels were immersed in 80 °C de-ionized water to selectively evaporate the hexane, and then freeze-dried to form an CCS aerogel with an ultralow density of 6.73 mg·cm^{-3} [71]. Similarly, Zhang et al. reported that the size distribution of GO emulsions and the resulting density of graphene monoliths could be controlled by concentrating the GO solution (Fig. 8) [19]. With increasing the concentration of GO, the average size of unit cells decreases with a narrower distribution. The resulting densities of graphene monolith ranged from 1.1 to 2.8 mg·cm^{-3}. Moreover, they reported improved mechanical properties of Young's modulus of 4.3 kPa at a density of 1.1 mg·cm^{-3} and a superior elastic stability

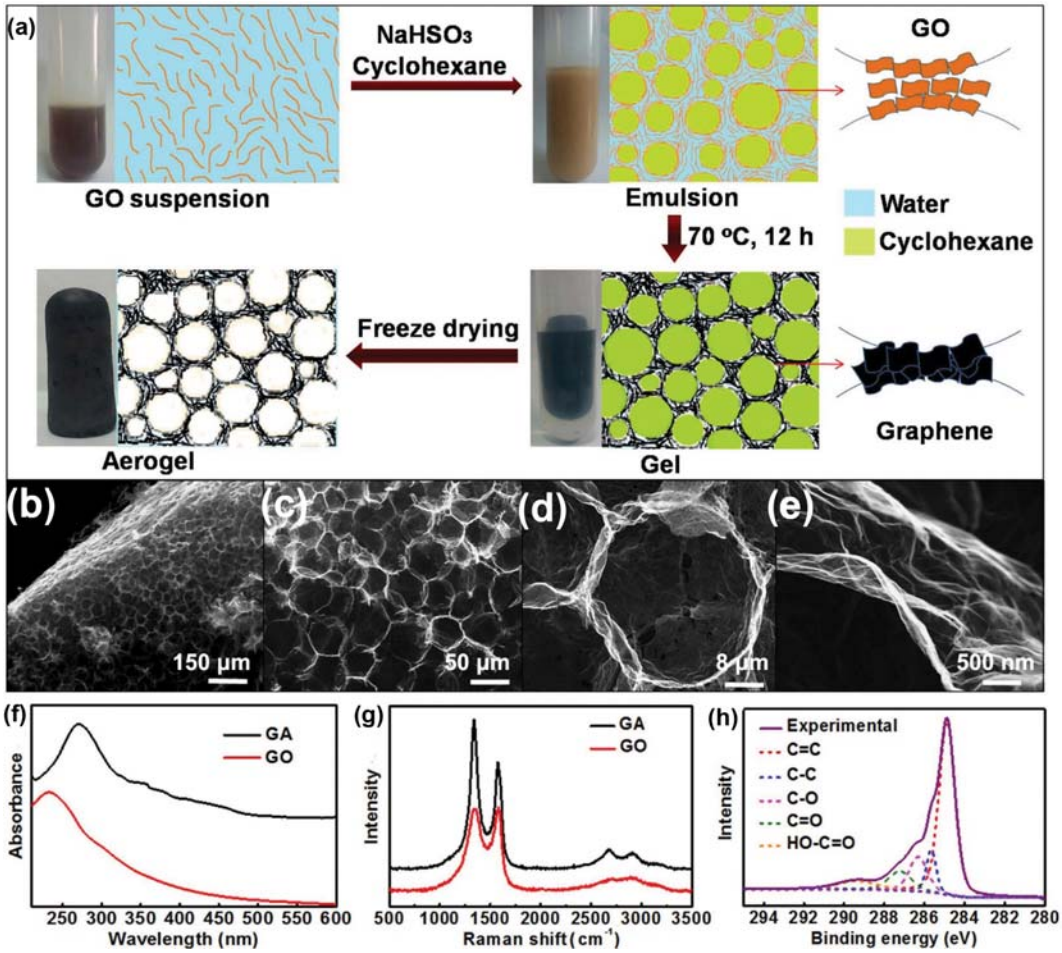

Fig. 8. Synthetic procedure and characterization of GA. (a) Scheme illustrating the synthetic process of GA from the assembly of GO at oil-water interface and the subsequent chemical reduction. (b) Macroscopic observation of GA derived from the emulsion with GO concentration of 2.0 mg·ml^{-1}, revealing that the bulk of aerogel is entirely composed of cellular-like pores. (c) Image showing closely linked pores with polyhedral morphology. (d) Hexagonal pore shares the boundary with other six adjacent pores, ensuring firm bridging for the interconnection. (e) The ultrathin and wrinkled wall structure. (f) UV-vis spectra of aqueous suspensions of GO and GA. (g) Raman spectra of GO and GA. (h) C 1s X-ray photoelectron spectroscopy spectrum of GA. Reproduced with permission from ref. [19]. Copyright 2016, Nature Publishing Group.

even with the excessive compressive strain up to 80%.

Several efforts have also been made while excluding the use of the hydrothermal method. Although an oil-in-water emulsion system was essentially utilized, a sequential method of freeze-drying and thermal reduction process could be adopted for structuring the graphene cellular network. For instance, Barg et al. demonstrated a mesoscale assembly of graphene into a closed cellular network, for which a mixture of GO solution including organic additives (sucrose or PVA) and toluene was emulsified [72]. The organic additives were added for further adjusting the architecture and physical properties of the assembled structure. The PVA molecules, an organic additive, could accelerate the emulsification and increase the stability of smaller emulsions. Likewise, sucrose served as a binder that would support to hold the cellular structures tightly even after the liquid is removed. Also, it affects the morphology of ice crystals during the unidirectional freezing process. The resulting closed cellular network showed lightweight densities ranging from 1 to 200 mg·cm^{-3} depending on the variation of the cell size (from ~7 to over 60 μm), thickness of the wall (from 1 to 100 nm), and the amount of organic additives. Furthermore, Ni et al. reported that the microscopic CCS could be predictably controlled by the size of the GO flakes [28]. The cellular structures made of larger-sized GO flakes (>20 μm) have shown superelastic properties of exhibiting high energy damping capability, much greater than those obtained from smaller sized GO flakes (<2 μm).

8. CCS: Wet-spinning with Coagulation

Wet-spinning method has successfully demonstrated the feasibility of generating superelastic and lightweight GA through one-step self-assembly of GOs in a facile way. Bead-like GAs were formed by the injection of droplets of GO solution in a coagulation bath. Although this example is classified as a CCS in this review, upon applying a strict structural evaluation, the bead-like material can be regarded as one type of core-shell structure. For instance, Bao et al. obtained GO beads using four different types of coagulating agents (calcium chloride, cetyltrimethylammonium bromide (CTAB), polyethylenimine (PEI), poly(diallyldimethylammonium chloride)

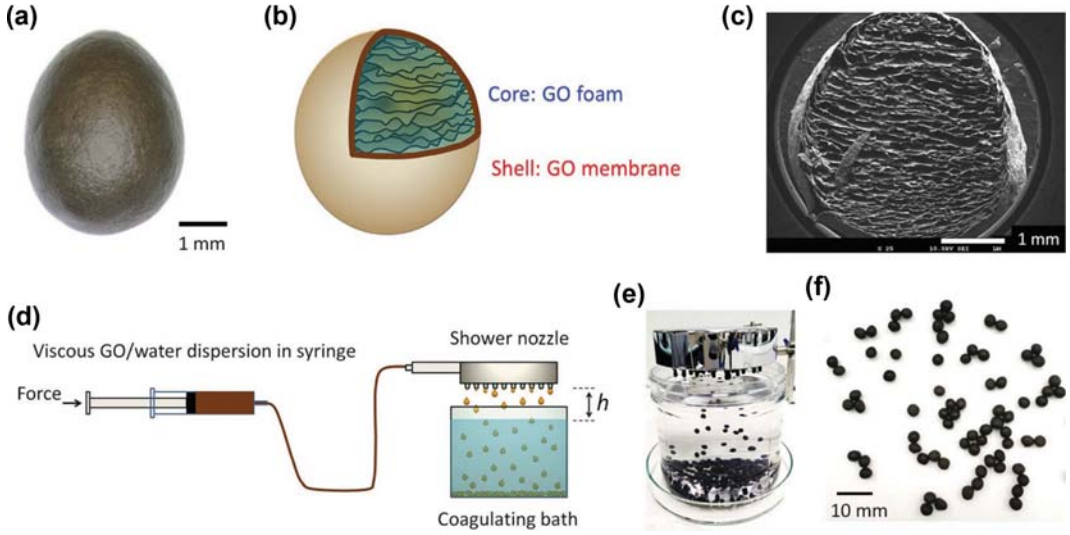

Fig. 9. (a) Optical microscopic image of a GO bead. (b) GO bead consists of a core/shell structure. (c) SEM image showing the cross section of a GO bead. (d) Illustration of the preparation set-up for GO bead synthesis; GO/water dispersions flow through the nozzle, form droplets, and drip into a coagulation bath. (e) Snapshot of the GO bead production. GO/water (1.5 wt%) droplets drip into the coagulation bath (1 wt% CTAB/water solution) and form GO beads. (f) Obtained GO beads. Reproduced with permission from ref. [73]. Copyright 2016, The Royal Society of Chemistry.

(PDDA)) [73]. In a preparation step, GO droplets were injected into a coagulation bath through the nozzle to form the GO beads (Fig. 9). Then, the injected GO droplets were cross-linked by the diffused coagulation agent and then freeze-dried. As a result, millimeter-sized GO beads could exhibit a Young's modulus of 345 kPa with a density of 20 $mg \cdot cm^{-3}$ and high energy absorption (1 $kJ \cdot kg^{-1}$) properties. In a similar manner, the realization of superelastic GA milli-spheres was reported by Zhao et al., especially using high temperature annealing process at 2,500 °C. As a result, unusually shaped core-shell structures with excellent elasticity (full recovery from a compression with 95% strain or a repetitive recovery from 1,000 cycles with 70% strain) and low densities (5.0-7.8 $mg \cdot cm^{-3}$) were obtained [74].

9. CCS: Sugar-blowing Method

Sugar-blowing is a simple synthetic method for preparing open or closed cellular polymer foams by employing physical or chemical blowing agents. As introduced in the related reviews, OCSs or CCSs can be implemented depending on material composition or

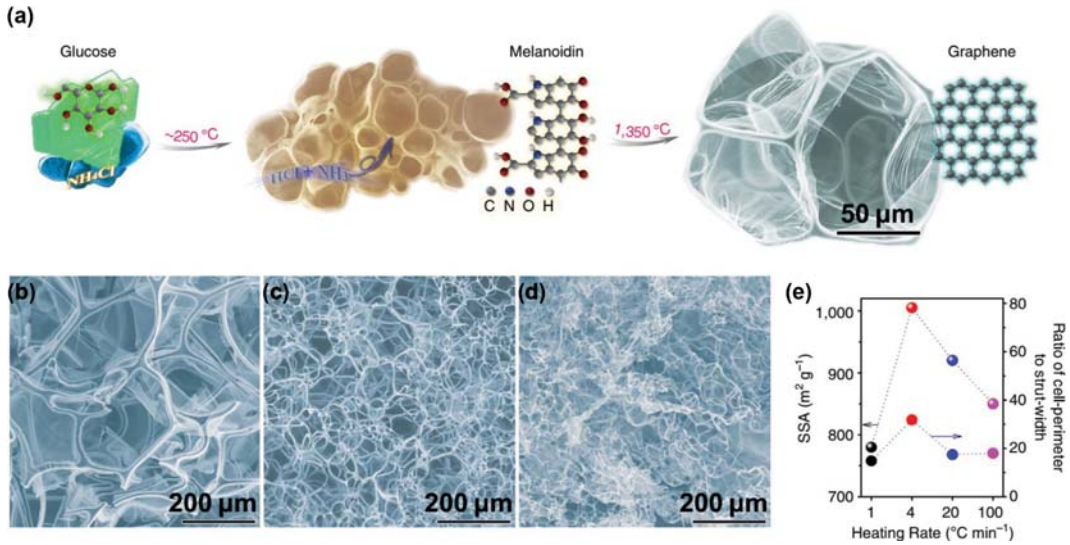

Fig. 10. (a) False colored SEM images of glucose (crystals colored in green) and NH_4Cl (in blue), which are subsequently transformed to melanoidin bubbles (in brown) under a browning reaction; these are finally converted into the strutted graphene containing graphitic membranes and struts (in gray). (b)-(d) SEM images of the strutted graphene products grown at the heating rates of 1, 20 and 100 °C·min^{-1}, respectively. (e) Changes of SSA and the ratio of cell perimeter to strut width versus heating rates. Reproduced with permission from ref. [77]. Copyright 2013, Nature Publishing Group.

foaming condition [75,76]. As an example of using the sugar-blowing method to create CCSs, Wang et al. demonstrated 3D self-supported GA using a mixture of glucose (or sugar) and NH_4Cl (Fig. 10) [77]. Heating a mixture transformed the mixed phase into a molten syrup, which then gradually polymerized and was blown with the released NH_3 gases (generated from thermally decomposing the NH_4Cl). The polymerized thin walls were subsequently graphitized into graphitic thin film (~2.2 nm) under thermal annealing at 1,350 °C. The as-prepared graphitic aerogel showed lightweight density of 3.0 mg·cm^{-3}, remarkable electrical conductivity of 0.6 S· m^{-1}, and structural recoverability against heavy compression up to 80%.

10. CCS: Microfluidic Generation

Microfluidic synthesis is an effective way to fabricate highly monodisperse emulsions or bubbles by utilizing multiple interfaces formed

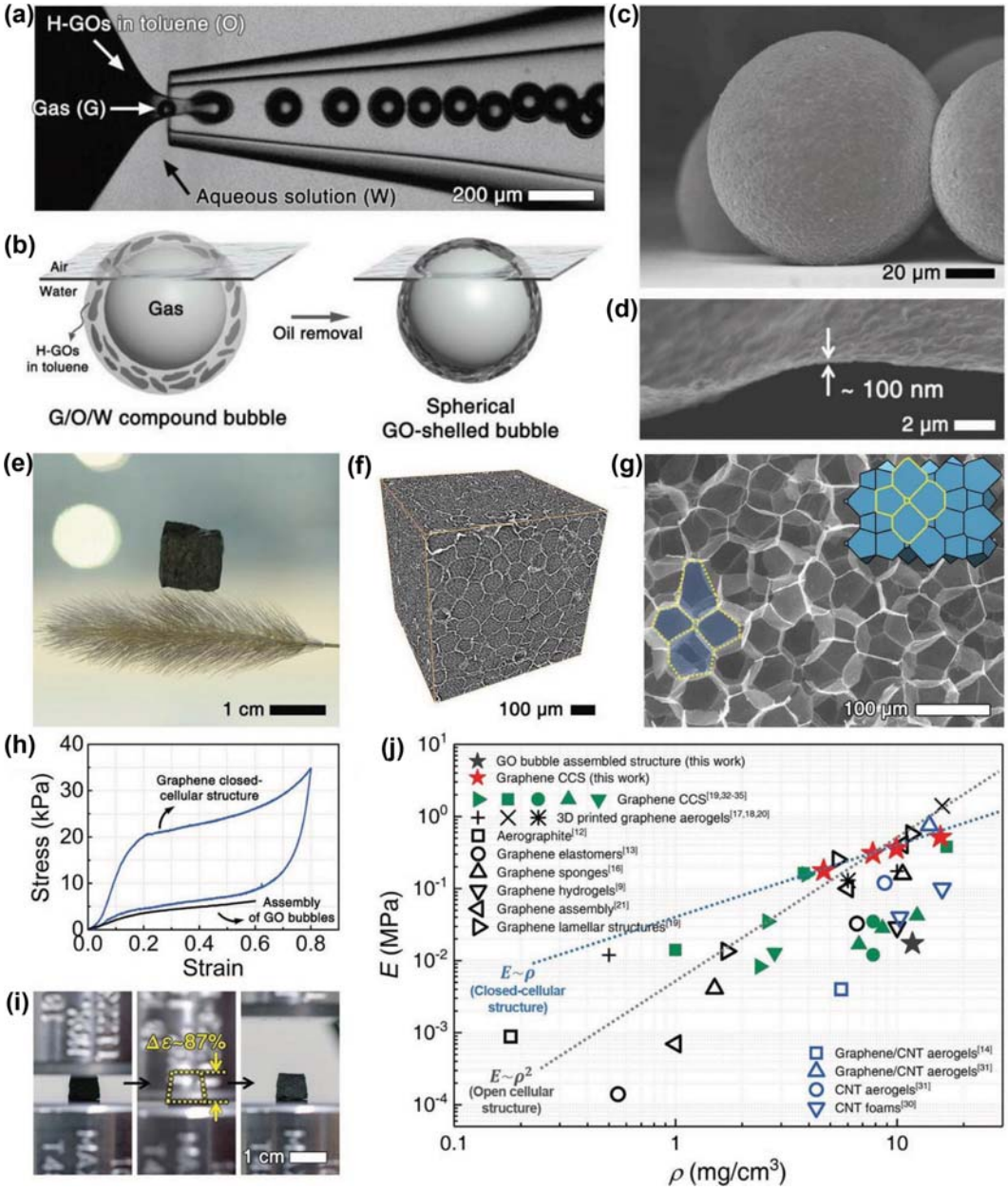

Fig. 11. Synthesis of microscale solid-shelled graphene bubbles. (a), (b) Optical microscopic image and schematic illustration of the formation of ultra-stable spherical microbubbles comprising highly-alkylated GO (H-GO) nanoplatelets. (c) SEM image of the microscale spherical H-GO-shelled bubbles. (d) Measurement of shell thickness of the bubble. (e) A digital photograph of the centimeter-scale 3D CCS of GO microbubbles placed on a green foxtail (after thermal reduction). (f) 3D reconstructed X-ray microtomographic images of the 3D assembly of thermally reduced H-GO-shelled microbubbles. (g) SEM image of the cross-section of 3D RDH structure. The inset shows an expected cross-view of ideal RDH structure. (h) Stress-strain curves of the 3D RDH structure (ρ=4.66 mg·cm^{-3}) and 3D assembly of H-GO-shelled microbubbles (ρ=11.7 mg·cm^{-3}). (i) Consecutive digital photographs showing the super-compressibility of the 3D RDH structure. (j) An Ashby plot for the 3D RDH structures compared to other carbon-based 3D porous structures (open- and closed-cellular). Reproduced with permission from ref. [80]. Copyright 2018, Wiley-VCH.

between immiscible phases. Generally, microfluidic devices are made of mold-replicated poly(dimethyl siloxane) (PDMS) or glass capillaries [78,79]. Emulsions or bubbles are continuously generated at the junction inside the microfluidic device, depending on the flow rate of each immiscible fluid. Since the interface formation between two immiscible fluids is the driving force for forming the particles or bubbles, when three or more immiscible phase are introduced, the resulting particles or bubbles are designed to have different internal and external components with more increased structural complexity.

Despite enormous efforts devoted so far, it remains a great challenge to attain the lightweight yet mechanically strong structures with superelasticity. Irregular size distribution of pores in the cellular networks is one of the biggest drawbacks for creating advanced structural materials due to the vulnerability to defect formation in emulsification-based synthetic methods. To address this issue, Yeo et al. reported a new method for creating graphene bubble-based closed cellular networks with a size/shape mono-dispersity in unit cells using microfluidic synthetic method (Fig. 11) [80]. For a microfluidic graphene bubble generation, GO nanosheets were alkyl-functionalized to impart the dispersibility in oil phase, which is necessary for stably segregating the oily GO phase from the outer aqueous phase. The highly monodispersed and ultra-stable (shelf life >1 year) GO shelled microbubbles were generated from gas-in-oil-in-water (G/O/W) compound microfluidic system and the collected bubbles were utilized as building units for assembling into the integrated closed cellular network. Using this bottom-up-based assembling approach, a specific concern on the size irregularity of unit cells in cellular network and the subsequent mechanical weakening could be substantially relieved. Also, the size and shell thickness of GO microbubbles and the resulting mechanical properties of bubble-assembled structures were readily controlled by altering the flow rates in microfluidic synthetic process.

Note that graphene microbubbles were closely packed into the ordered 2D hexagonal or 3D face-centered cubic (FCC) assembled structures at the water-air interface spontaneously by buoyancy and capillary attraction. More intriguingly, those assembled structures could be transformed into 2D honeycomb or 3D rhombic dodecahedral honeycomb (RDH) shaped CCSs using thermal reduction process. Since the reduction reaction induces the interfacial bonding between adjacent faces of graphene microbubbles, stack-assembled spherical bubbles were transformed into plesiohedron-shaped unit cells. Accordingly, this structural transformation could reinforce the interconnectivity between unit cells and result in a dramatic improvement in mechanical strength and elasticity. The resulting plesiohedral CCSs presented a lightweight density of 4.66 $mg{\cdot}cm^{-3}$ with a corresponding Young's modulus of 177 kPa, while securing the superelasticity with a full recovery upon applying compressive strain of 87%. In consequence, the well-defined periodic CCSs can provide advanced mechanical properties as well as ultralow density and superelastic characteristics as compared to conventional carbon-based OCSs or CCSs.

APPLICATIONS OF GRAPHENE-BASED 3D LIGHTWEIGHT CELLULAR STRUCTURES

Graphene-based 3D cellular structures are composed of 2D graphene/GO nanosheets, which naturally inherit the superior physical properties of graphene, including strong mechanical strength/flexibility (~1 TPa) [9], good electrical conductivity and a huge SSA (~2,630 $m^2{\cdot}g^{-1}$), and a wide range of light absorption [1,2,6,7]. Furthermore, hierarchical 3D cellular structures usually exhibit enhanced physical properties with multi-dimensional electrical pathways [81], structural flexibility/superelasticity as well as largely expanded SSA for surface reaction in electrochemical systems [82,83]. Harnessing these attractive physical properties, graphene-based 3D cellular structures have shown more advanced performances in wide range of applications than those obtained from conventional carbon-based structured materials. In this chapter, we further highlight the applications of graphene based-lightweight cellular structures particularly for environmental and electrochemical uses, including energy storage, photocatalysts, sensors, liquid absorption, and other applications.

1. Energy Storage

Graphene based 3D cellular structures have been considered as highly competent materials for energy storage and conversion applications because of their unique physical properties, such as high electrical conductivity, electrochemical stability, greatly extended SSA, mechanical durability, and mechanical responsiveness (superelasticity) of the interconnected graphene networks. For example, ultrathin graphite foam having a density ~9.5 $mg{\cdot}cm^{-3}$, prepared by template-directed CVD method, showed remarkably high electrical conductivity of 1.3×10^5 $S{\cdot}m^{-1}$ at room temperature [84]. Used as a cathode for lithium ion batteries, the maximum specific capacity of the ultrathin graphite foam was observed as 102 $mA{\cdot}h{\cdot}g^{-1}$ with a high rate capability without exhibiting any parasitic anodic current in the potential range of 2-5 V. This result is indicative of excellent electrochemical stability and reversibility with high open-circuit voltage. To develop more effective GA-based cathodes, the introduction of tetrahydroxyl-1,4-benzoquinone (THQ) during GA synthetic procedure has been considered [85]. The strong reducing ability of THQ would enable the self-assembled formation of 3D GA from the dispersion of GOs. At the same time, electrochemically inactive oxygen groups on the surface of GO are transformed into redox-active oxygen functional groups by THQ. The resulting functionalized GA electrodes could exhibit high gravimetric capacities of ~165 $mA{\cdot}h{\cdot}g^{-1}$ in Li ion cells and ~120 $mA{\cdot}h{\cdot}g^{-1}$ in Na ion cells. In another approach, Liu et al. reported polydopamine-coated GAs prepared by hydrothermal reduction process of a mixture of GO and dopamine [86], by which the polymerized dopamine promoted the charge storage properties for both Li- and Na-ion storage. This was attributed to the presence of oxygen atoms in o-benzoquinone group of polydopamine that facilitated the replacement of proton with lithium or sodium ions. Also, the superheated condition of water and the proton generation during hydrothermal condition effectively suppressed the isolated generation of by-product of polydopamine particles [87].

Furthermore, graphene-based 3D cellular structures have been widely utilized as high-performance electrodes for supercapacitors. For instance, Xu et al. reported self-assembled graphene hydrogel prepared by a facile one-step hydrothermal synthesis with electrical conductivity as high as 5×10^{-3} $S{\cdot}cm^{-1}$ [43]. The resulting specific capacitance of the self-assembled graphene hydrogel was meas-

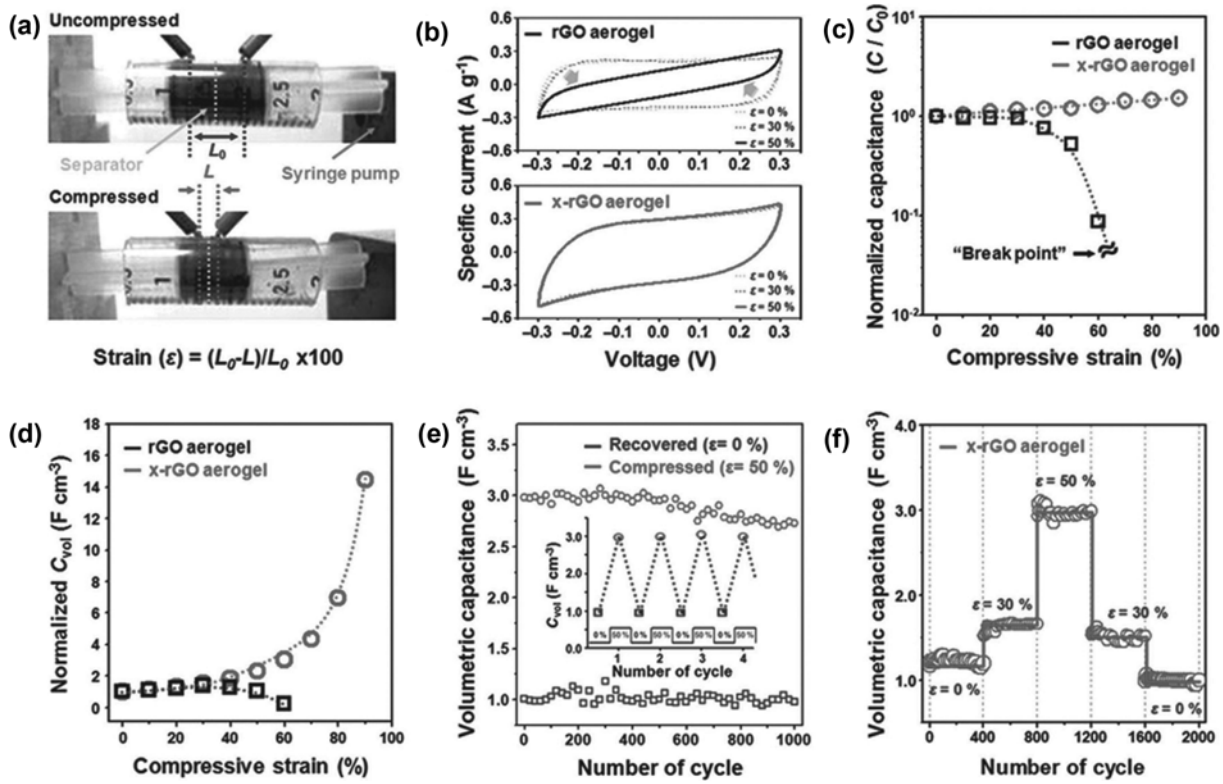

Fig. 12. (a) Digital photographs of the two-electrode measurement device under different compression states. (b) Comparison between cyclic voltammetry curves of rGO aerogel (top) and cross-linked-rGO aerogel (bottom) in original and compressed states (ε=30 and 50%). (c) Normalized gravimetric capacitance (C/C_0) and (d) volumetric capacitance (C_{vol}) of rGO aerogel (black) and cross-linked-rGO aerogel (red) at compressive strains in the range of 0 to 90%. (e) The C_{vol} of cross-linked-rGO aerogel under sequentially repeated compression and relaxation for 1,000 cycles. (f) Stability test of cross-linked-rGO aerogel. Cycle performance test showing a capacitance retention >84.5% even after 2,000 charging/discharging cycles under constant compression strains of 0, 30, and 50%. Reproduced with permission from ref. [16]. Copyright 2015, Wiley-VCH.

ured to be 175 and 152 $F \cdot g^{-1}$ at potential scan rates of 10 and 20 $mV \cdot s^{-1}$, respectively. In addition, Zhao et al. presented hydrothermally synthesized N-doped graphene frameworks with a density of 2.1±0.3 $mg \cdot cm^{-3}$ for supercapacitors [54]. The resulting structures showed high conductivity of $1.2\pm0.2\times10^3$ $S \cdot m^{-1}$ and high specific capacitance of 484 $F \cdot g^{-1}$ (at a current density of 1 $A \cdot g^{-1}$); thanks to the synergetic effect of 3D OCS formation with N-doping. Worsley et al. reported 3D graphene macro-assembly using sol-gel synthesis for supercapacitors application [88]. The assembled structures exhibited high energy density (27 $W \cdot h \cdot kg^{-1}$), power density (10 $kW \cdot kg^{-1}$), and large capacitance (165 $F \cdot g^{-1}$ at a scan rate of 1 $mV \cdot s^{-1}$). Likewise, Wang et al. showed 3D strutted graphene networks, grown by sugar blowing method, especially for supercapacitors with high-power-density [77]. The 3D strut interconnections could implement not only generating electronic/phononic pathways but also prevent the disintegration or restacking of graphitic membranes. Thus, this 3D strutted graphene networks showed overall high conductivity of 1 $S \cdot m^{-1}$ even under a heavy compression up to 80%. Also, the resulting observed capacitance was as high as 250 $F \cdot g^{-1}$ at 1 $A \cdot g^{-1}$, and its maximum power density of strutted graphene was 893 $kW \cdot g^{-1}$ at 100 $A \cdot g^{-1}$. Hong et al. also developed reversibly compressible, highly elastic, and durable GAs using cross-linking chemistry and freeze-drying method [16]. The resulting cross-linked rGO aerogel has 240% greater capacitance (295 $F \cdot g^{-1}$) than that of non-crosslinked rGO aerogel (122 $F \cdot g^{-1}$) (Fig. 12). In response to applying the programmed compressive strains, the initially obtained gravimetric capacitance (110 $F \cdot g^{-1}$) of the cross-linked rGO aerogel was minimally changed. Also, the capacitance value could be maintained by 84.5% (93 $F \cdot g^{-1}$) even after 2,000 charge/discharge cycles under 1 $A \cdot g^{-1}$. Furthermore, the volumetric capacitances reversibly changed in the range from 1.19 to 2.97 $F \cdot cm^{-3}$ according to the degree of applying compressive strains (from 0 to 50%) due to the outstanding elasticity and mechanical durability of the cross-linked rGO aerogels.

In addition to electrical energy storage applications of GAs, several strategies have also been proposed to use GAs for storing heat energy. The key process is to form the composites by immersing phase-change materials (PCMs) into GAs. Due to their high porosity and surface area characteristics, GAs can absorb the PCM uniformly inside the structure. Notably, the transport of heat flow was highly facilitated on account of a high thermal conductivity of the GA scaffold. Yang et al. reported GA microstructure by combining CVD and self-assembly methods, followed by the hybridization of GA with paraffin wax as PCMs [89]. This hybridization approach successfully improved the form shape stability while securing low thermal conductivity, which has been a common drawback

of PCMs. Compared to pure paraffin wax, the thermal conductivity of the GA-PCMs hybridized composite was found to be improved by 574%. As for an extended approach, fiber-shaped GAs/PCMs coated with hydrophobic fluorocarbon resin were also reported as phase-changing smart fibrous material [90]. The resulting fibers showed highly extended thermal stability under a wide range of phase transition temperature and the applied heat energy (0-186 $J \cdot g^{-1}$).

2. Photocatalyst

Light absorption, photogenerated charge separation, and transfer to active materials in the surface reaction process are recognized as key steps for facilitating photo-induced redox reactions [91]. In addition, good electrical conductivity, hierarchically developed electron transport pathways, superior adsorption capacity by highly porous structure, and abundant presence of functional groups on large SSA of graphene-based 3D cellular structures are important properties for implementing high performance photocatalytic systems [92]. Although the application area of photocatalysts is enormously wide, we would like to focus on recent strategies associated with environmental remedies by considering the importance of nanocarbons as the environmentally benign next generation high performance material.

GA-based photocatalysts with excellent recyclability supported by structural durability have been investigated for removing toxic ions or organic pollutants in water. Fan et al. reported hydrothermally synthesized AgX/GAs (X=Br, Cl) for efficient photocatalytic degradation of water pollutants. The photocatalytic degradation characteristics were confirmed through two different degradation processes: oxidative degradation of organic pollutants and subsequent reduction of Cr^{4+} [93]. As for more practical examples, Tsang et al. demonstrated benzothiadiazole (BTZ)-copolymer loaded GAs as a metal-free visible light photocatalyst for the photodecomposition of organic dyes [94]. This work drew significant attention in terms of direct utilization of visible light, instead of conventionally used UV-based photocatalysts [95]. They introduced BTZ-based conjugated microporous polymers as photocatalytic material that was flexibly tuned to absorb light in the visible wavelength range, thanks to their unique properties of extensive organic π-conjugation [96]. The resulting BTZ (5 wt%)-GAs exhibited notably enhanced light absorbance and corresponding photocatalytic activity in removing organic pollutants greater than 90% under an irradiation of visible light for 80 min, which surpassed the performances of other GA-based photocatalysts under the same reaction condition.

In addition to removal of water pollutants, strategies have been developed to degrade harmful gas molecules in air. Yang et al. reported $BiVO_4$ (BVO) quantum tubes (QTs)-loaded GAs for the degradation of gaseous formaldehyde [97]. Since GAs had good mechanical strength, high SSA and electrical conductivity, they were able to maximize the photocatalytic properties of BVO-QTs, resulting in a degradation of formaldehyde from 1.0 ppm to 0.4 ppm in 15 min. Zhang et al. reported graphitic carbon nitride (g-C_3N_4) loaded GAs, which showed efficient photooxidation of NO with a max removal ratio of 45.9% [98]. Moreover, g-C_3N_4/GAs exhibited photoreduction reactions of CO_2 with CO, CH_4 and H_2 with production rates of 42.9, 4.6 and 1.6 $\mu mol \cdot g^{-1} \cdot h^{-1}$, respectively. Furthermore, they reported Pd-embedded g-C_3N_4/GAs using one-pot thermal reduction method [99]. The resulting Pd-g-C_3N_4/GAs showed improved hydrogenation performance of CO_2 to CH_4 with a maximum CH_4 evolution rate of 6.4 $\mu mol \cdot g^{-1} \cdot h^{-1}$, which is 12.8-fold enhancement than that obtained from a use of pure g-C_3N_4.

Likewise, solar-driven water splitting has become one of the most promising routes as renewable energy utilization, which is significant in terms of simultaneous accomplishments of solar energy storage and green production of H_2 [100]. GAs not only provide the huge SSA by which the photocatalysts are homogeneously distributed with a high areal density, but also possess effective electron pathways to support the photocarrier transport [91]. Lu et al. reported hydrothermally synthesized GAs as a robust photocatalyst for H_2 production via water splitting under the wavelength range of UV-visible light by employing a hot electron transfer mechanism [101]. The bare GAs exhibited an H_2 production rate of 270 $\mu mol \cdot h^{-1} \cdot g_{cat}^{-1}$. Whereas, TiO_2/GA composite achieved a H_2 production rate of 1,205 $\mu mol \cdot h^{-1} \cdot g_{cat}^{-1}$ and a 7.2% of apparent quantum efficiency at 350 nm. Basically, the observed quantum efficiency in the water splitting process is greater than that obtained from bare GAs or TiO_2 by an order of magnitude due presumably to the following three mechanisms: (a) hot/free electrons can be generated efficiently by graphene and GAs [102], (b) photo-generated electron transfer at the interface of graphene and TiO_2 occurs several times faster than electron-phonon energy relaxation [103], and (c) GAs can reduce the bandgap of anatase phase of TiO_2 and accordingly increases the electron transfer from the Fermi level of GAs to the lower conduction band of TiO_2, and suppresses the recombination of photogenerated electron-hole pairs [104]. Pan et al. demonstrated rGO-NiS_2/g-C_3N_4 aerogel using continuous thermal oxidation etching-hydrothermal method to obtain dual co-catalyst modified aerogels [105]. The resulting rGO-NiS_2 modified g-C_3N_4 aerogel shows 67-times higher H_2 production rate (~1555.34 $\mu mol \cdot g^{-1} \cdot h^{-1}$) than that of pristine g-C_3N_4 aerogel (~23.13 $\mu mol \cdot g^{-1} \cdot h^{-1}$), due primarily to the Pt-like electrochemical properties of NiS_2. NiS_2 acted as electron acceptor for transferring the photon-generated electrons for accelerating the carrier separation. Also, 2D-structured rGOs with high conductivity provided good electrical pathways to transfer the photon-generated electrons to the solution for promoting the H_2 production.

3. Sensors

Graphene-based 3D cellular structures can accurately measure externally applied stimuli with monitoring the structural deformation and resulting changes in electrical resistance. Therefore, the materials previously discussed possess suitable structural benefits for uses as strain sensors owing to their good elasticity, mechanical durability, and electrical sensitivity in response to the structural deformation. For instance, Li et al. reported electrical resistance changes upon compressing rGO monoliths prepared by emulsified hydrothermal synthesis up to 30% strain [71]. They showed highly stable resistance responses during the repeated compression with 300 times. Kuang et al. demonstrated that thermally-reduced graphene foams prepared by directional freeze-drying method could exhibit piezo-resistive behavior due to its hierarchical structure [40]. The resulting rGO foams presented not only excellent compression-recovery feature but also linear piezo-resistive behavior along

the in-plane direction up to 60% strain. Impressively, unlike conventional strain-gauge sensors, the rGO foams could work successfully under extreme temperature conditions (–50, 25, and 200 °C) without sacrificing the properties of rapid response time and high endurance against the deformation. Based on these characteristics, the feasibility of rGO foam sensors as a health monitoring system was successfully demonstrated.

Chen et al. reported flexible and conductive interconnected-3D graphene foams using CVD method [8]. To impart good flexibility, PDMS was introduced to form the flexible composite with the graphene foam. The resulting composites could freely be bent, stretched and twisted without causing any breakage. Notably, the electrical resistance increased only ~2.7% after 10,000 folding/unfolding cycles with a bending radius of 2.5 mm. Also, the resistance rarely changed according to the applied strain before exceeding the strain value of 60%. Qin et al. presented rGO/PI nanocomposite aerogel-based strain sensors using freeze-drying and thermal annealing method [29]. The mechanically fragile rGO aerogels were modified by complexing the PI, forming highly flexible and elastic nanocomposite aerogels. As a result, rGO/PI aerogels showed synergistically improved effect, including good electrical conductivity (~2.2×10^{-2} S·m^{-1}), compression sensitivity, and excellent durability even after 2,000 compression-recovery cycles (Fig. 13). In addition, rGO/PI nanocomposites could be formed to have a desired shape with varying the shape of freeze-drying mold. In this way, for example, a ribbon-like structured composite foam could exert delicate sensing capability against the bending and torsion deformations as well as simple compression or stretching. Ho et al. also

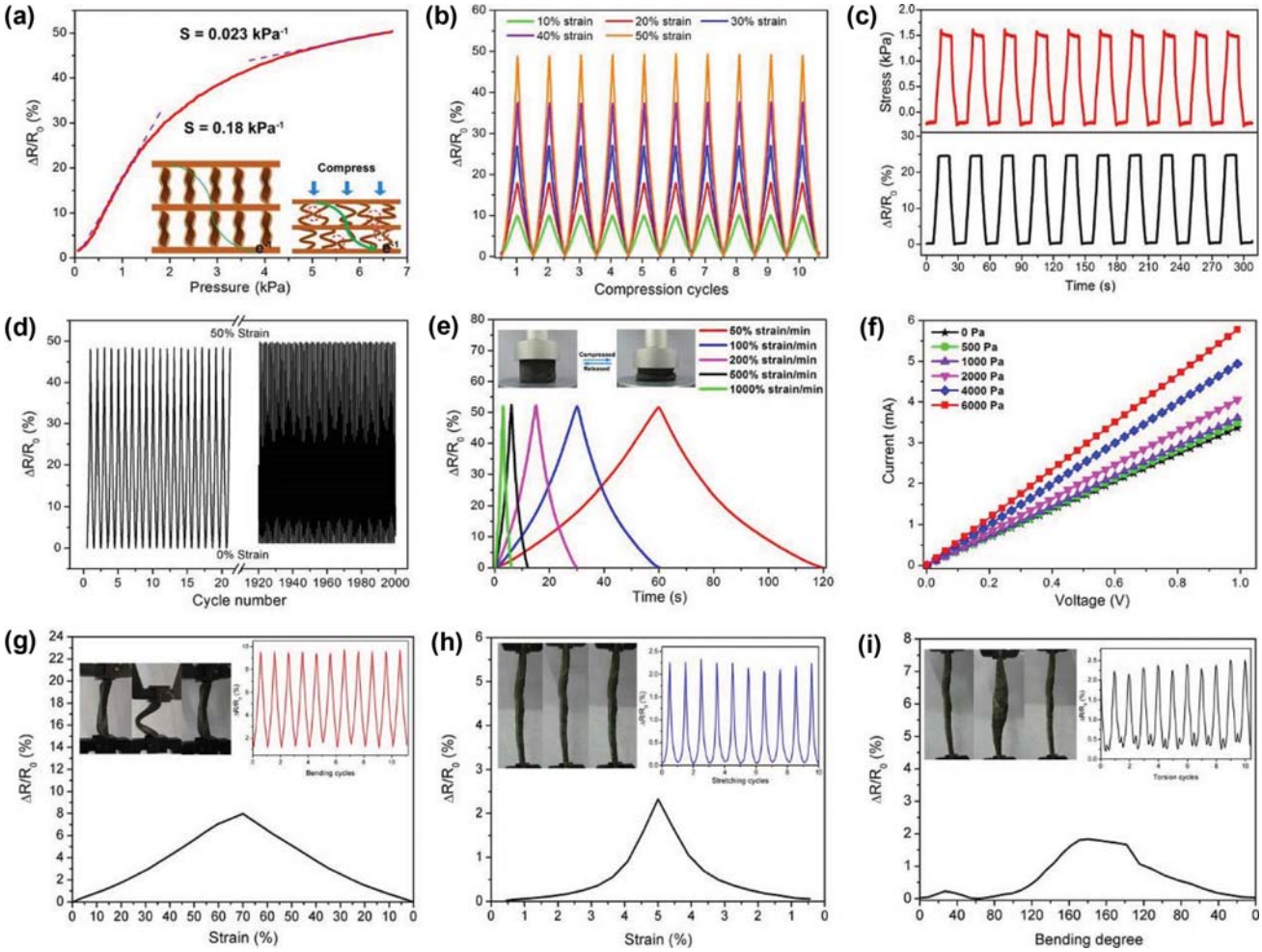

Fig. 13. (a) Pressure-response curves for rGO/PI nanocomposite. Inset is a schematic showing current changes in response to the compression and release. (b) Multiple-cycle tests of changes in resistance with different applied strains. (c) The time retention curves of changes in resistance and stress with time. (d) Cycling stability test of rGO/PI composite under repeated applied strain of 50% for 2,000 cycles. (e) Variation of the resistance of the rGO/PI composite with the strain of 50% under different strain rates (50-1,000%·min^{-1}). (f) Current-voltage relationship of rGO/PI nanocomposites under different applied stress. (g) The resistance variation of the rGO/PI nanocomposite in a typical bending cycle. Inset: applying under mechanical deformation of bending and straightening for each cycle. (h) Electrical-resistance change of rGO/PI nanocomposite as a function of stretching strain of 5%. Inset: applying after 5% stretching and then releasing for each cycle. (i) Electrical-resistance variation of rGO/PI nanocomposite in a typical torsion cycle. Inset: applying after 180 degree torsion and then releasing for each cycle. Reproduced with permission from ref. [29]. Copyright 2015, American Chemical Society.

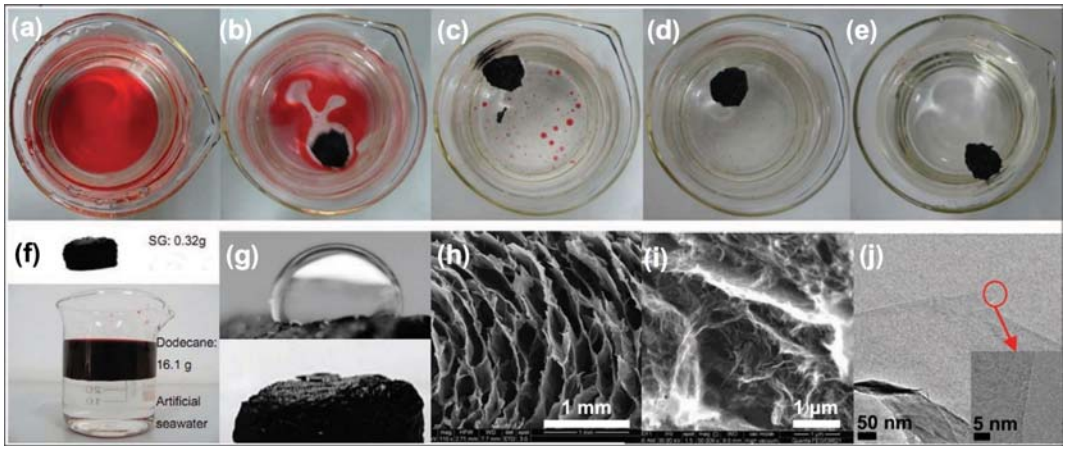

Fig. 14. Oil absorption properties of GAs. (a)-(e) Absorption of dodecane in spongy graphene at intervals of 20 s. Dodecane (stained with Sudan red 5B) floating on artificial seawater is completely absorbed within 80 s. (f) Efficiency of oil absorption. A GA bulk block with a mass of 0.32 g absorbs 16.1 g dodecane floating on water, corresponding to a weight gain of 50.3. (g) Contact angle of GA surface (upper panel) and fast absorption of dodecane (lower panel). The contact angle to water is 114°±2°, but dodecane is quickly absorbed without any residue remaining on the surface. (h) SEM image of the microporous (fusiform) structure of GA. (i) SEM image of the graphene skeleton. (j) TEM image of the graphene skeleton. Reproduced with permission from ref. [24]. Copyright 2012, Wiley-VCH.

demonstrated ultra-lightweight strain-responsive 3D graphene network by using multiscale assembly and self-interconnections of ~100 μm-sized graphene solid bubbles [106]. Since the interconnection process was induced by thermal reduction process, the resulting CCS aerogels exhibited different gauge factors according to the degree of reduction reaction. Using a calculation, they revealed that the difference in tunneling distance between stacked rGO nanosheets would influence the gauge factor in strain measurements. Consequently, a strain gauge with a gauge factor of ~4 could be demonstrated when the rGO aerogels were fully reduced under high temperature reduction process. Furthermore, the aerogels exhibited excellent mechanical durability over 250 cycles.

Alternatively, Zhang et al. developed a one-step preparation method of generating 3D rGO assemblies using a reducing agent for the application of distinguishing organic solvents by polarity difference [48]. In particular, the rGO/PDMS composite was proposed as an effective sensor for a detection of organic solvents. Interestingly, the observed current values were precipitously reduced upon applying the solvent (generally within several seconds). This was due to an increase in the resistance of the composite according to the swelling of PDMS matrix. The drop in the current value was more pronounced with increasing the relative polarity of the solvent; for example, the reported relative polarity of ethanol, acetone, and chloroform was 0.654, 0.355, and 0.259, respectively. After the evaporation of the immersed solvent, accordingly, the current value recovered to its initial state and the sensing procedure could be managed completely reversible. Similarly, 3D printed graphene lattices fabricated by Zhang et al. also presented sensing detection performance for organic solvents [67]. The binding of solvent molecules to rGO sheets could influence the charge transfer characteristics, which would be distinctly monitored by corresponding increase in the resistance.

4. Liquid Absorption

The important physical properties of graphene-based 3D cellular structures can be generated from huge SSA, ultra-low density, excellent mechanical properties, and good chemical stability. Since these structured materials can readily be prepared as a form of free-standing films, they can effectively be used as the absorbent for organic or inorganic contaminants from the source of pollution. Also, the absorbed contaminants are easily released and separated by mechanically squeezing the graphene foam. As an example, Bi et al. developed a graphene-based sponge as a highly efficient and recyclable absorbent for oils and organic solvents (Fig. 14) [24]. The resulting spongy graphene showed massive yet quick absorption of oils (up to 86-times of its own weight), exhibiting greater efficiency (>10 times) than that of conventional foam absorbers. Also, spongy graphene could be reused more than 10-times through heat treatment while maintaining a high efficiency of oil removal (>99%).

Similarly, several studies have been reported for liquid absorption. Fluorinated GAs reported by Hong et al. exhibited not only high absorption of oils or organic solvents (more than 100 times of its own weight) but also indicated a good reusable capability [53]. Also, Sun et al. demonstrated a highly prompt absorption process of spilled toluene solvent over water using the ultra-flyweight aerogel only within 5 s [41]. Remarkably high absorption capacity of ultra-flyweight aerogel (up to 320 times of its own weight) was two-orders of magnitude greater than that of commercially used absorption materials. Barg et al. reported closed-cellular GAs with excellent organic absorption capability (up to 605-times of its own weight) [72]. These closed-cellular GAs were introduced in the previous section on the emulsified freeze-drying method. Due to their remarkable mechanical and chemical stability, the organic solvent or oil could readily be released from the cellular GA absorber by mechanical compressing. The structurally recovered GAs were reused over several cycles without sacrificing the liquid absorption capability (>95% of the initial absorption amount). Notably, Wu et al. reported that GAs (also introduced in the section of hy-

drothermal synthesis) could exhibit extremely high liquid absorption capacity (up to 1,010-times of its own weight) and structural stability (recovery against the compression up to 98%) for repeated uses [44]. Since the ultralight GA could be solvothermally synthesized with ethanol based low concentration and large-sized GO solution (0.20-5.00 $mg \cdot ml^{-1}$, ~20 to 50 μm in lateral dimension), the absorbed liquid can be compressed out completely from GA in seconds, and absorption/release process is highly repeatable without any structural degradation even after hundreds of cycles. As another approach to improve liquid absorbing performance, Wang et al. suggested using bi-directional freeze-drying for improving the structural alignment inside GAs [107]. In conventional freeze-drying for directional alignment, the growth direction of the ice crystals is set in the z-axis direction only, from the bottom to the top. On the other hand, bi-directional freeze-drying method employs a copper tube with cylindrical hole inside to contain GO solution, such that ice crystals could grow radially with the shape of lamellae during freezing process initiated from cold side walls to center. In a combination of concurrently working capillary forces resulting from both vertically and radially aligned superstructure, the bi-directional freeze-drying of GAs has shown the greatest absorption capacity among three different types of representative aerogels: GAs prepared from bi-directional, unidirectional, or common freezing method.

Moreover, Liu et al. demonstrated efficient absorption of organic liquids using anisotropically structured GAs (up to 200-times of its own weight) while applying three different types of recycling method: burning, distilling, and squeezing [50]. Due to their good thermal stability, the resulting GAs showed mostly retained absorption efficiency (~10% reduction in absorption capability) even after applying 10 cycles of absorption/burning removal, during which a slight volume shrinkage was observed in GAs. Similarly, absorbed organic liquid could be vaporized from the GAs by distilling it at a temperature near the boiling point that would also ensure the stable absorption capability for repeated uses. In addition, Bao et al. presented GO beads with a core/shell structure (core: GO foam, shell: GO membrane) for a fast absorption of hazardous chemicals such as concentrated strong acid or base solutions [73]. Notably, the outer shelled membrane helped to keep the absorbed corrosives inside the beads and prevent secondary leakage, whereas the inner core foam could absorb sulfuric acid as much as 44-times its own weight. Due to the amphiphilicity of GO and porous cellular structure of the core, GO beads could rapidly absorb a variety of hazardous chemicals (only 1 min for sulfuric acid). In the case of sulfuric acid (97% concentrated), for example, GO beads could absorb it 44-times of its own weight only within 1 min. The chemical stability of the GO beads was also remarkable; no changes in the appearance and structure were observed for 60 min even with fully absorbing sulfuric acid inside.

5. Other Applications

In addition to the above introduced application areas (energy storage, photocatalyst, sensors, and liquid absorption), the graphene-based 3D cellular structures are also expected to be utilized for other purposes. For example, along with advances in nano- and micro-structuring technology, structurally well-defined graphene-based materials can be used as a building unit for their assembled networks to create excellent physical properties of mechanical reinforcement or energy damping [52]. By applying this strategy to graphene-based CCSs, the assembly of uniform-sized graphene bubbles generated from microfluidic synthetic process has greatly improved the structural homogeneity of the assembled networks. It has been generally regarded as highly irregular and random in their internally assembled structures due to the excessive incorporation of non-uniform sized pores [80]. Therefore, minimizing the structural defects and non-uniformity in the network structures is the most important key to achieve the enhanced physical and mechanical properties. As another means to improve mechanical properties of GAs, a method of hybridizing with shape memory polymer (SMP) was also suggested [108]. Despite notable advantages of SMPs, such as low cost, high energy efficiency, large deformation (up to 800%), easy processability, and degradability compared to conventional shape memory alloys (SMAs), they generally suffered from slow response time (~ a few minutes) as a result of retarded viscoelasticity of SMP chains, which was much slower than that of SMAs (less than 1 s) [109-111]. However, graphene/SMP nanocomposite aerogel could exhibit a relatively fast response ($175 \pm 40\ mm \cdot s^{-1}$), large deformation (~100%), and a wide response bandwidth (0.1-20 Hz). In particular, shortened heat transmission distance in SMP nanofilms and the rapid electrothermal conversion of the graphene framework simultaneously implemented not only fast response time (50 ms at the minimum) but also durable cyclability and high recovery ratio (98%) of graphene/SMP nanocomposite aerogel.

Interesting works exploiting the intrinsic thermoelectric properties of GAs have been also reported. Xie et al. reported free-standing and chemically reduced GA films exhibiting excellent bolometric properties in vacuum [112]. [A bolometer is a type of microdevice for thermal imaging, which absorbs infrared, visible, or ultraviolet light from the objects and converts them into electrical signals to indicate the temperature variation.] With remarkably low thermal conductivity (6.0-0.6 $mW \cdot m^{-1} \cdot K^{-1}$ from 295 to 10 K), high porosity, ultralight density (4 $mg \cdot cm^{-3}$), and populated presences of nitrogen and oxygen-containing functional groups, GO-based ultralight GAs have implemented excellent bolometric performance [113]. Likewise, Li et al. developed highly efficient cylindrical cryo-thermocells using anisotropically holey GA-structured electrodes [114]. Unlike bolometers, a thermocell is a thermal energy harvester that can convert temperature-dependent electrochemical redox potentials into electrical power. In general, thermocell devices are weakened in their energy harvesting performance under low temperature due to subsequently lowered ion conductivity of electrolytes. To challenge this limitation, they introduced the formamide-mixed electrolyte into the anisotropic holey GA. The formamide aqueous mixture could impart high ion conductivity as well as much lowered operation temperature down to - 40 °C. In addition, anisotropic holey-structured GA electrodes rendered highly enhanced ion conductivity supported by the alignments of graphene sheets and internal pores [115]. Thanks to these synergistic improvements, the power density and Seebeck coefficient of a single cylindrical GA thermocell could show superior thermoelectric properties of 3.6 $W \cdot m^{-2}$ and 1.3 $mV \cdot K^{-1}$, respectively.

Furthermore, GAs have found their way to serve as materials

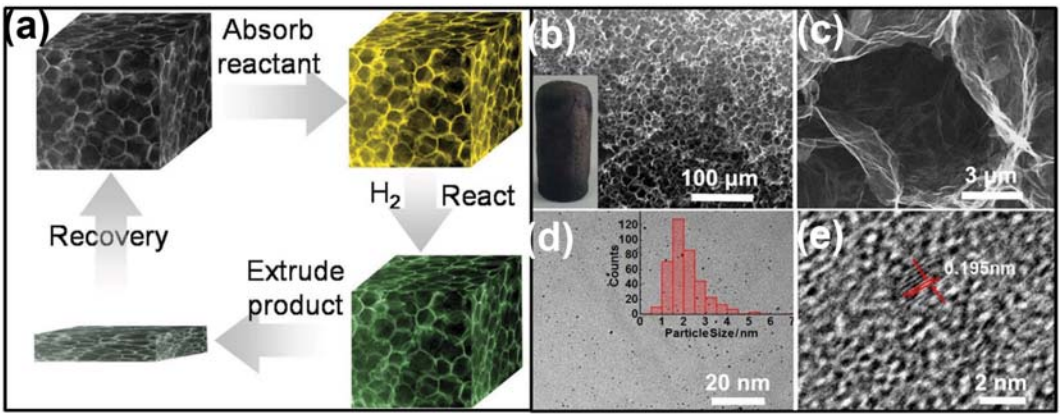

Fig. 15. Application for the catalytic hydrogenation using Pd/GA. (a) The illustration showing catalytic hydrogenation using GA as a reactor. (b) SEM image of the Pd/GA, the inset shows a photograph of the Pd/GA monolith with an integral structure. (c) Magnified SEM image of cell structure in Pd/GA. (d) TEM image of graphene sheet of the wall bearing Pd nanoparticles. The inset shows the size distribution of Pd nanoparticles. (e) High-resolution TEM image of Pd/GA reveals the lattice spacing of about 0.195 nm, corresponding to the lattice fringe of Pd (2 0 0). Reproduced with permission from ref. [19]. Copyright 2016, Nature Publishing Group.

for electromagnetic interference (EMI) shielding due to their high electrical/thermal conductivity, excellent mechanical properties, flexibility, and high aspect ratio [116-118]. Representatively, there have been a number of reports on the improvement in EMI shielding effectiveness using graphene, complexed with highly conductive metallic species, such as iron, silver and copper [119-121]. Meanwhile, Xi et al. reported that the excellent EMI shielding performance of GA films was obtained by freely expanding rGO films with multilayer structures, namely, employing the expansion enhancement effect (EEE) [122]. Intriguingly, they identified the changes in EMI shielding efficiency depending on the compression ratio of the sample; a 1.4 mm-thick sample showed EMI shielding effectiveness of ~135 dB in 0.1-3 GHz, whereas a compressed 0.3 mm-thick sample showed the effectiveness of ~105 dB. Nevertheless, the intrinsic electrical conductivity and the areal density maintained as constant. Therefore, they suggested that the optimized control of EEE could effectively improve the EMI shielding effectiveness. Besides the contribution from EEE, the multilayered and directionally aligned GA films imparted superior EMI shielding properties than randomly structured graphene foams or graphene composites, because the closed and layered structure along the direction of the wave transmission could effectively interrupt the wave propagation. The resulting GA films have shown remarkably high EMI shielding effectiveness (~135 dB in 0.1-3 GHz at thickness of 1.4 mm and 65 to 105 dB in 2-18 GHz at thickness of 120 μm) and superior properties in the thickness-averaged specific shielding effectiveness (~100,000 $dB \cdot cm^2 \cdot g^{-1}$).

Furthermore, extremely high SSA and mechanical durability of graphene-based cellular networks can infuse great advantages for the applications in hydrogenation catalytic reactors (Fig. 15) [19]. The highly interconnected porous structures would facilitate the mass diffusion along with high absorption capability for organic reactants and facile separation of product. Also, mechanically responsive and compressible features enabled the regeneration of GAs, repeatedly. In addition, graphene or its derivatives have shown great potential for flame retardant applications while simultaneously securing thermal and gas barrier properties [123]. The graphene lattice structures prepared by 3D printing method sustained a stable flame retardancy even with applying 30 min combustion test (Fig. 16) [67]. Furthermore, more effective flame-retardant properties were

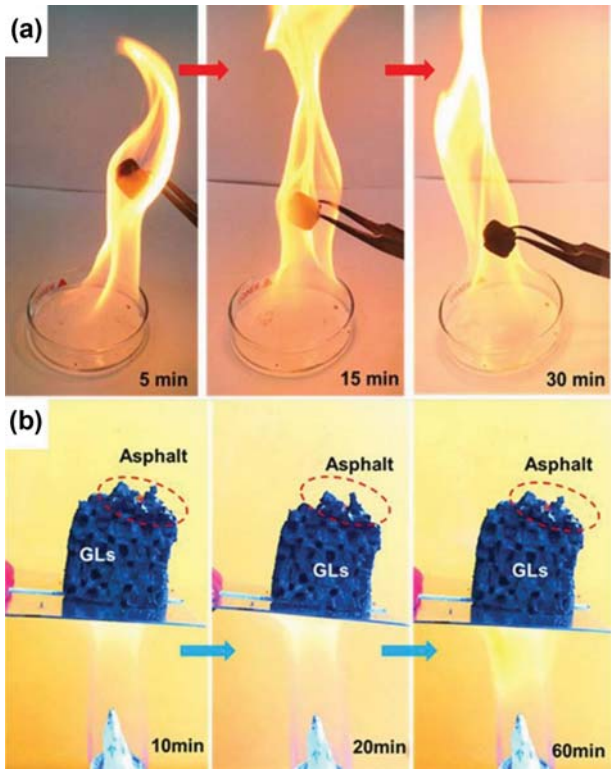

Fig. 16. (a) Digital photographs showing fireproof for 30 min combustion in air. (b) Thermal insulation investigation for graphene lattices heated at the bottom to identify the absorption inhibition performances of top-applied semisolid asphalt. Reproduced with permission from ref. [67]. Copyright 2018, American Chemical Society.

reported when the GO was complexed with cellulose nanofiber and silicate nanorods, which are well-known as excellent flame-retardant species [124].

CONCLUSIONS

We have introduced examples of the fabrication method of graphene-based 3D lightweight cellular structures and their emerging applications. First, we classified the cellular structures, especially in the regime of ultra-lightweight materials (<10 mg·cm^{-3}), as OCSs or CCSs according to the internal pore interconnectivity. The synthetic methods, such as freeze-drying, hydrothermal, chemical reducing/crosslinking, sol-gel, template-directed CVD, and 3D printing, were representatively introduced as a toolkit for creating graphene-based OCSs. However, the implementation of CCSs using graphene materials has been relatively limited due to the technological difficulty in generating constituting unit cells with isolated domains. Nevertheless, some methods have been proposed to overcome this intrinsic limitation, such as by employing emulsified hydrothermal/freeze-drying, wet-spinning with coagulation, sugar blowing, and microfluidic generation. With further developments in effective fabrication methods, the graphene-based lightweight cellular structures have evolved into more advanced high-performance materials. Subsequently, in the second part, emerging applications of graphene-based 3D lightweight cellular structures were discussed, particularly for energy storage, sensors, and liquid absorption applications by highlighting their advantages of huge SSA, high electrical conductivity, facile functionality, mechanical durability, and super elasticity.

However, there are still some challenges to maximizing the potential of graphene-based cellular structures. Notably, most of introduced examples of graphene-based 3D lightweight cellular structures have shown wide distribution in their unit cell size and wall thickness, and irregular porosity, which would eventually act as structural defects with undermining the mechanical stability and elasticity of the structured materials. Therefore, there should be further advances in improving the structural uniformity of graphene-based cellular structures to fully secure the structural and physical properties. To this end, fundamental mechanical studies and theoretical simulations must be accompanied to realize the ideal cellular structures, which will also offer a valuable solution to maximize the required properties even in limited circumstances in material selection. Finally, considering commercialization, it is mandatory to improve the processability for mass production of graphene-based cellular structures. In most of the approaches developed so far, we are still facing problems of high-cost yet small-yield production. Toward the realization of the next generation structural, transportation, and electrical industrial applications, it is very important to develop more efficient designing and fabrication tools for producing graphene-based cellular structured materials with scalability.

ACKNOWLEDGEMENTS

This work was supported by a grant (19SCIP-B146646-02) from the Construction Technology Research Project funded by the Ministry of Land, Infrastructure and Transport (MLIT), Korea.

REFERENCES

1. M. D. Stoller, S. Park, Y. Zhu, J. An and R. S. Ruoff, *Nano Lett.*, **8**, 3498 (2008).
2. C. N. R. Rao, A. K. Sood, K. S. Subrahmanyam and A. Govindaraj, *Angew. Chem. Int. Ed.*, **48**, 7752 (2009).
3. A. A. Balandin, S. Ghosh, W. Bao, I. Calizo, D. Teweldebrhan, F. Miao and C. N. Lau, *Nano Lett.*, **8**, 902 (2008).
4. K. I. Bolotin, K. J. Sikes, Z. Jiang, M. Klima, G. Fudenberg, J. Hone, P. Kim and H. L. Stormer, *Solid State Commun.*, **146**, 351 (2008).
5. Y. B. Zhang, Y. W. Tan, H. L. Stormer and P. Kim, *Nature*, **438**, 201 (2005).
6. F. Bonaccorso, Z. Sun, T. Hasan and A. C. Ferrari, *Nat. Photonics*, **4**, 611 (2010).
7. Y. Guan, T. Hu, J. Wu, L. Zhao, F. Tian, W. Pan, P. He, X. Qi, F. Li and K. Xu, *Korean J. Chem. Eng.*, **39**, 115 (2016).
8. Z. Chen, W. Ren, L. Gao, B. Liu, S. Pei and H. Cheng, *Nat. Mater.*, **10**, 424 (2011).
9. C. Lee, X. Wei, J. W. Kysar and J. Hone, *Science*, **321**, 5887 (2008).
10. D. Li, M. B. Muller, S. Gilje, R. B. Kaner and G. G. Wallace, *Nat. Nanotechnol.*, **3**, 101 (2008).
11. S. Stankovich, D. A. Dikin, R. D. Piner, K. A. Kohlhaas, A. Kleinhammes, Y. Jia, Y. Wu, S. T. Nguyen and R. S. Ruoff, *Carbon*, **45**, 1588 (2007).
12. X. Li, W. Cai, J. An, S. Kim, J. Nah, D. Yang, R. Piner, A. Velamakanni, I. Jung, E. Tutuc, S. K. Banerjee, L. Colombo and R. S. Ruoff, *Science*, **324**, 1312 (2009).
13. D. C. Marcano, D. V. Kosynkin, J. M. Berlin, A. Sunitskii, Z. Sun, A. Slesarev, L. B. Alemany, W. Lu and J. M. Tour, *ACS Nano*, **4**, 4806 (2010).
14. J.-H. Lee, E. K. Lee, W.-J. Joo, Y. Jang, B.-S. Kim, J. Y. Lim, S.-H. Choi, S. J. Ahn, J. R. Ahn, M.-H. Park, C.-W. Yang, B. L. Choi, S.-W. Hwang and D. Whang, *Science*, **344**, 286 (2014).
15. Z. Chen, W. Ren, L. Gao, B. Liu, S. Pei and H.-M. Cheng, *Nat. Mater.*, **10**, 424 (2011).
16. J. Y. Hong, B. M. Bak, J. J. Wie, J. Kong and H. S. Park, *Adv. Funct. Mater.*, **25**, 1053 (2015).
17. S. C. Kim, K. P. Young, B. H. Kim, H. Kim, J. L. Won, H. Lee and S. C. Jung, *Korean J. Chem. Eng.*, **35**, 750 (2018).
18. S. K. Park, P. Nakhanivej and H. S. Park, *Korean J. Chem. Eng.*, **36**, 1557 (2019).
19. B. Zhang, J. Zhang, X. Sang, C. Liu, T. Luo, L. Peng, B. Han, X. Tan, X. Ma, D. Wang and N. Zhao, *Sci. Rep.*, **6**, 25830 (2016).
20. T. T. K. Huynh, T. Q. N. Tran, H. H. Yoon, W.-J. Kim and I. T. Kim, *Korean J. Chem. Eng.*, **36**, 1193 (2019).
21. M. A. E. F. Barakat, R. Kumar, N. H. A. Makishah, A. A. Neamtallah and Z. O. Alafif, *Korean J. Chem. Eng.*, **36**, 1281 (2019).
22. F. Abbasi, J. Karimi-Sabet, C. Ghotbi and Z. Abbasi, *Korean J. Chem. Eng.*, **35**, 1174 (2018).
23. M. J. Noh, M. J. Oh, J. H. Choi, J. C. Yu, W. J. Kim, J. Park, Y. W. Chang and P. J. Yoo, *Soft Matter*, **14**, 6708 (2018).
24. H. Bi, X. Xie, K. Yin, Y. Zhou, S. Wan, L. He, F. Xu, F. Banhart, L. Sun and R. S. Ruoff, *Adv. Funct. Mater.*, **22**, 4421 (2012).
25. T. S. Kazeem, M. Zubair, M. Daud, N. D. Mu'azu and M. A. A.

Harthi, *Korean J. Chem. Eng.*, **36**, 1057 (2019).
26. F. Tahmasebi, M. Alimohammadi, R. Nabizadeh, M. Khoobi, K. Karimian and A. Zarei, *Korean J. Chem. Eng.*, **6**, 894 (2019).
27. H. Mirzazadeh and M. Lashanizadegan, *Korean J. Chem. Eng.*, **35**, 684 (2018).
28. N. Ni, S. Barg, E. Garcia-Tunon, F. M. Perez, M. Miranda, C. Lu, C. Mattevi and E. Saiz, *Sci. Rep.*, **5**, 13712 (2015).
29. Y. Qin, Q. Peng, Y. Ding, Z. Lin, C. Wang, Y. Li, F. Xu, J. Li, Y. Yuan, X. He and Y. Li, *ACS Nano*, **9**, 8933 (2015).
30. K. S. Kim, S. R. Lim, S. E. Kim, J. Y. Lee, C. H. Chung, W. S. Choe and P. J. Yoo, *Sens. Actuators B Chem.*, **242**, 1121 (2017).
31. Y. Lee, J. Kim, J. H. Koo, T.-H. Kim and D.-H. Kim, *Korean J. Chem. Eng.*, **35**, 1 (2018).
32. K. S. Novoselov, E. McCann, S. V. Morozov, V. I. Falko, M. I. Katsnelson, U. Zeitler, D. Jiang, F. Schedin and A. K. Geim, *Nat. Phys.*, **2**, 177 (2006).
33. K. S. Kim, Y. Zhao, H. Jang, S. Y. Lee, J. M. Kim, K. S. Kim, J.-H. Ahn, P. Kim, J.-Y. Choi and B. H. Hong, *Nature*, **457**, 706 (2009).
34. D. Wan, C. Yang, Y. Tang, M. Zhou, Y. Zhong, F. Huang and J. Lin, *ACS Nano*, **6**, 9068 (2012).
35. L. J. Gibson, M. F. Ashby and B. A. Harley, Cellular Materials in Nature and Medicine, Cambridge University Press, Cambridge, UK (2010).
36. L. J. Gibson, *J. Biomech.*, **38**, 377 (2005)
37. T. A. Schaedler, A. J. Jacobsen, A. Torrents, A. E. Sorensen, J. Lian, J. R. Greer, L. Valdevit and W. B. Carter, *Science*, **334**, 962 (2011).
38. N. Hüsing and U. Schubert, *Angew. Chem., Int. Ed.*, **37**, 22 (1998).
39. A. C. Pierre and G. M. Pajonk, *Chem. Rev.*, **102**, 4243 (2002).
40. J. Kuang, L. Liu, Y. Gao, D. Zhou, Z. Chen, B. Han and Z. Zhang, *Nanoscale*, **5**, 12171 (2013).
41. H. Sun, Z. Xu and C. Gao, *Adv. Mater.*, **25**, 2554 (2013).
42. Y. Zhou, Q. Bao, L. A. L. Tang, Y. Zhong and K. P. Loh, *Chem. Mater.*, **21**, 2950 (2009).
43. Y. Xu, K. Sheng, C. Li and G. Shi, *ACS Nano*, **4**, 4324 (2010).
44. Y. Wu, N. Yi, L. Huang, T. Zhang, S. Fang, H. Chang, N. Li, J. Oh, J. A. Lee, M. Kozlov, A. C. Chipara, H. Terrones, P. Xiao, G. Long, Y. Huang, F. Zhang, L. Zhang, X. Lepró, C. Haines, M. D. Lima, N. P. Lopez, L. P. Rajukumar, A. L. Elias, S. Feng, S. J. Kim, N. T. Narayanan, P. M. Ajayan, M. Terrones, A. Aliev, P. Chu, Z. Zhang, R. H. Baughman and Y. Chen, *Nat. Commun.*, **6**, 7141 (2015).
45. L. Qiu, J. Z. Liu, S. L. Y. Chang, Y. Wu and D. Li, *Nat. Commun.*, **3**, 1241 (2012).
46. C. A. Hunter and J. K. M. Sanders, *J. Am. Chem. Soc.*, **112**, 5525 (1990).
47. W. Chen and L. Yan, *Nanoscale*, **3**, 3132 (2011).
48. L. Zhang, G. Chen, M. N. Hedhili, H. Zhanga and P. Wang, *Nanoscale*, **4**, 7038 (2012).
49. X. Zhang, Z. Sui, B. Xu, S. Yue, Y. Luo, W. Zhanc and B. Liuc, *J. Mater. Chem.*, **21**, 6494 (2011).
50. T. Liu, M. Huang, X. Li, C. Wang, C.-X. Gui and Z.-Z. Yu, *Carbon*, **100**, 456, (2016).
51. X. Xie, Y. Zhou, H. Bi, K. Yin, S. Wan and L. Sun, *Sci. Rep.*, **3**, 2117 (2013).
52. H. Hu, Z. Zhao, W. Wan, Y. Gogotsi and J. Qiu, *Adv. Mater.*, **25**, 2219 (2013).
53. J. Y. Hong, E. H. Sohn, S. Park and H. S. Park, *Chem. Eng. J.*, **269**, 229 (2015).
54. Y. Zhao, C. Hu, Y. Hu, H. Cheng, G. Shi and L. Qu, *Angew. Chem. Int. Ed.*, **51**, 11371 (2012).
55. S. Vinod, C. S. Tiwary, P. A. da Silva Autreto, J. Taha-Tijerina, S. Ozden, A. C. Chipara, R. Vajtai, D. S. Galvao, T. N. Narayanan and P. M. Ajayan, *Nat. Commun.*, **5**, 4541 (2014).
56. L. L. Hence and J. K. West, *Chem. Rev.*, **90**, 33 (1990).
57. M. A. Worsley, P. J. Pauzauskie, T. Y. Olson, J. Biener, J. H. Satcher Jr. and T. F. Baumann, *J. Am. Chem. Soc.*, **132**, 14067 (2010).
58. M. A. Worsley, T. Y. Olson, J. R. I. Lee, T. M. Willey, M. H. Nielsen, S. K. Roberts, P. J. Pauzauskie, J. Biener, J. H. Satcher and T. F. Baumann, *J. Phys. Chem. Lett.*, **2**, 921 (2011).
59. F. Meng, X. Zhang, B. Xu, S. Yue, H. Guo and Y. Luo, *J. Mater. Chem.*, **21**, 18537 (2011).
60. A. Reina, X. Jia, J. Ho, D. Nezich, H. Son, V. Bulovic, M. S. Dresselhaus and J. Kong, *Nano Lett.*, **9**, 30 (2009).
61. M. Mecklenburg, A. Schuchardt, Y. K. Mishra, S. Kaps, R. Adelung, A. Lotnyk, L. Kienle and K. Schulte, *Adv. Mater.*, **24**, 3486 (2012).
62. H. Bi, I. W. Chen, T. Q. Lin and F. Q. Huang, *Adv. Mater.*, **27**, 5943 (2015).
63. E. García-Tuñon, S. Barg, J. Franco, R. Bell, S. Eslava, E. D'Elia, R. C. Maher, F. Guitian and E. Saiz, *Adv. Mater.*, **10**, 1688 (2015).
64. C. Zhu, T. Y. J. Han, E. B. Duoss, A. M. Golobic, J. D. Kuntz, C. M. Spadaccini and M. A. Worsley, *Nat. Commun.*, **6**, 6962 (2015).
65. Y. Lin, F. Liu, G. Casano, R. Bhavsar, I. A. Kinloch and B. Derby, *Adv. Mater.*, **28**, 7993 (2016).
66. Zhang, F. Zhang, S. P. Medarametla, H. Li, C. Zhou and D. Lin, *Small*, **12**, 1702 (2016).
67. Q. Zhang, F. Zhang, X. Xu, C. Zhou and D. Lin, *ACS Nano*, **12**, 1096 (2018).
68. J. Kim, L. J. Cote, F. Kim, W. Yuan, K. R. Shull and J. X. Huang, *J. Am. Chem. Soc.*, **132**, 8180 (2010).
69. F. Kim, L. J. Cote and J. X. Huang, *Adv. Mater.*, **22**, 1954 (2010).
70. Z. Sun, T. Feng and T. P. Russell, *Langmuir*, **29**, 13407 (2013).
71. Y. Li, J. Chen, L. Huang, C. Li, J.-D. Hong and G. Shi, *Adv. Mater.*, **26**, 4789 (2014).
72. S. Barg, F. M. Perez, N. Ni, P. do Vale Pereira, R. C. Maher, E. Garcia-Tuñon, S. Eslava, S. Agnoli, C. Mattevi and E. Saiz, *Nat. Commun.*, **5**, 4328 (2014).
73. C. Bao, S. Bi, H. Zhang, J. Zhao, P. Wang, C. Y. Yue and J. Yang, *J. Mater. Chem. A*, **4**, 9437 (2016).
74. X. Zhao, W. Yao, W. Gao, H. Chen and C. Gao, *Adv. Mater.*, **29**, 1701482 (2017).
75. M. Inagaki, J. Qiu and Q. Guo, *Carbon*, **87**, 128 (2015).
76. S. Costeux, *J. Appl. Polym. Sci.*, **131**, 41293 (2014).
77. X. Wang, Y. Zhang, C. Zhi, X. Wang, D. Tang, Y. Xu, Q. Weng, X. Jiang, M. Mitome, D. Golberg and Y. Bando, *Nat. Commun.*, **4**, 2905 (2013).
78. J. C. McDonald and G. M. Whitesides, *Acc. Chem. Res.*, **35**, 491 (2002).
79. R. K. Shah, H. C. Shum, A. C. Rowat, D. Lee, J. J. Agresti, A. S. Utada, L. Y. Chu, J. W. Kim, A. Fernandez-Nieves, C. J. Martinez and D. A. Weitz, *Mater. Today*, **11**, 18 (2008).
80. S. J. Yeo, M. J. Oh, H. M. Jun, M. Lee, J. G. Bae, Y. Kim, K. J. Park, S. Lee, D. Lee, B. M. Weon, W. B. Lee, S. J. Kwon and P. J. Yoo, *Adv. Mater.*, **30**, 1802997 (2018).

81. G. Tang, G. Jiang, X. Li, H. Zhang, A. Dasari and Z. Yu, *Carbon*, **77**, 592 (2014).
82. Q. Zhang, Y. Wang, B. Zhang, K. Zhao, P. He and B. Huang, *Carbon*, **127**, 449 (2018).
83. C. Li, D. Jiang, H. Liang, B. Huo, C. Liu, W. Yang and J. Liu, *Adv. Funct. Mater.*, **28**, 1704674 (2018).
84. H. X. Ji, L. L. Zhang, M. T. Pettes, H. F. Li, S. S. Chen, L. Shi, R. Piner and R. S. Ruoff, *Nano Lett.*, **12**, 2446 (2012).
85. T. Liu, R. Kavian, I. Kim and S. W. Lee, *J. Phys. Chem. Lett.*, **5**, 4324 (2014).
86. T. Liu, B. Lee, B. G. Kim, M. J. Lee, J. Park and S. W. Lee, *Small*, **14**, 1801236 (2018).
87. W. Zheng, H. Fan, L. Wang and Z. Jin, *Langmuir*, **31**, 11671 (2015).
88. M. A. Worsley, S. O. Kucheyev, H. E. Mason, M. D. Merrill, B. P. Mayer, J. Lewicki, C. A. Valdez, M. E. Suss, M. Stadermann, P. J. Pauzauskie, J. H. Satcher, J. Biener and T. F. Baumann, *Chem. Commun.*, **48**, 8428 (2012).
89. J. Yang, G.-Q. Qi, R.-Y. Bao, K. Yi, M. Li, L. Peng, Z. Cai, M.-B. Yang, D. Wei and W. Yang, *Energy Storage Mater.*, **13**, 88 (2018).
90. G. Li, G. Hong, D. Dong, W. Song and X. Zhang, *Adv. Mater.*, **30**, 1801754 (2018).
91. K.-Q. Lu, X. Xin, N. Zhang, Z.-R. Tang and Y.-J. Xu, *J. Mater. Chem.* A, **6**, 4590 (2018).
92. X. Li, J. Yu, S. Wageh, A. A. Al-Ghamdi and J. Xie, *Small*, **12**, 6640 (2016).
93. Y. Fan, W. Ma, D. Han, S. Gan, X. Dong and L. Niu, *Adv. Mater.*, **27**, 3767 (2015).
94. C. H. A. Tsang, J. Tobin, J. Xuan, F. Vilela, H. B. Huang and D. Y. C. Leung, *Appl. Catal. B*, **240**, 50 (2019).
95. C. Hou, Q. Zhang, Y. Li and H. Wang, *J. Hazard. Mater.*, **205**, 229 (2012).
96. Y.-L. Wong, J. M. Tobin, Z. Xu and F. Vilela, *J. Mater. Chem. A*, **4**, 18677 (2016).
97. J. Yang, Q. Shi, R. Zhang, M. Xie, X. Jiang, F. Wang, X. Cheng and W. Han, *Carbon*, **138**, 118 (2018).
98. R. Zhang, M. Ma, Q. Zhang, F. Dong and Y. Zhou, *Appl. Catal. B*, **235**, 17 (2018).
99. R. Zhang, Z. Huang, C. Li, Y. Zuo and Y. Zhou, *Appl. Surf. Sci.*, **475**, 953 (2019).
100. X. Li, J. Yu, J. Low, Y. Fang, J. Xiao and X. Chen, *J. Mater. Chem. A*, **3**, 2485 (2015).
101. Y. Lu, B. Ma, Y. Yang, E. Huang, Z. Ge, T. Zhang, S. Zhang, L. Li, N. Guan, Y. Ma and Y. Chen, *Nano Res.*, **10**, 1662 (2017).
102. Y. Lu, Y. Yang, T. Zhang, Z. Ge, H. Chang, P. Xiao, Y. Xie, L. Hua, Q. Li and H. Li, *ACS Nano*, **10**, 10507 (2016).
103. R. Long, N. J. English and O. V. Prezhdo, *J. Am. Chem. Soc.*, **134**, 14238 (2012).
104. Y. Yan, C. Wang, X. Yan, L. Xiao, J. He, W. Gu and W. Shi, *J. Phys. Chem. C*, **118**, 23519 (2014).
105. J. Pan, B. Wang, Z. Dong, C. Zhao, Z. Jiang, C. Song, J. Wang, Y. Zheng and C. Li, *Int. J. Hydrogen Energy*, **44**, 19942 (2019).
106. D. H. Ho, H. M. Jun, S. J. Yeo, P. Hong, M. J. Oh, B. M. Weon, W. B. Lee, S. J. Kwon, P. J. Yoo and J. H. Cho, *J. Phys. Chem. C*, **123**, 9884 (2019).
107. C. H. Wang, X. Chen, B. Wang, M. Huang, B. Wang, Y. Jiang and R. S. Ruoff, *ACS Nano*, **12**, 5816 (2018).
108. F. Guo, X. Zheng, C. Liang, Y. Jiang, Z. Xu, Z. Jiao, Y. Liu, H. T. Wang, H. Sun, L. Ma, W. Gao, A. Greiner, S. Agarwal and C. Gao, *ACS Nano*, **13**, 5549 (2019).
109. A. Lendlein and S. Kelch, *Angew. Chem., Int. Ed.*, **41**, 2034 (2002).
110. Z. L. Wang, *Mater. Today*, **10**, 20 (2007).
111. Y. Ogawa, D. Ando, Y. Sutou and J. Koike, *Science*, **353**, 368 (2016).
112. Y. Xie, M. Han, R. Wang, H. Zobeiri, X. Deng, P. Zhang and X. Wang, *ACS Nano*, **13**, 5385 (2019).
113. X. Mu, X. Wu, T. Zhang, D. B. Go and T. Luo, *Sci. Rep.*, **4**, 3909 (2014).
114. G. Li, D. Dong, G. Hong, L. Yan, X. Zhang and W. Song, *Adv. Mater.*, **31**, 1901403 (2019).
115. H. Sun, L. Mei, J. Liang, Z. Zhao, C. Lee, H. Fei, M. Ding, J. Lau, M. Li, C. Wang, X. Xu, G. Hao, B. Papandrea, I. Shakir, B. Dunn, Y. Huang and X. Duan, *Science*, **356**, 599 (2017).
116. D. D. L. Chung, *Carbon*, **39**, 279 (2001).
117. Z. Fang, C. Li, J. Sun, H. Zhang and J. Zhang, *Carbon*, **45**, 2873 (2007).
118. Z. Chen, C. Xu, C. Ma, W. Ren and H. M. Cheng, *Adv. Mater.*, **25**, 1296 (2013).
119. S. Wu, M. Zou, Z. Li, D. Chen, H. Zhang, Y. Yuan, Y. Pei and A. Cao, *Small*, **14**, 1800634, (2018).
120. Y. Huangfu, C. Liang, Y. Han, H. Qiu, P. Song, L. Wang, J. Kong and J. Gu, *Compos. Sci. Technol.*, **169**, 70 (2019).
121. X. Liu, T. Chen, H. Liang, F. Qin, H. Yang and X. Guo, *RSC Adv.*, **9**, 27 (2019).
122. J. Xi, Y. Li, E. Zhou, Y. Liu, W. Gao, Y. Guo, J. Ying, Z. Chen, G. Chen and C. Gao, *Carbon*, **135**, 44 (2018).
123. C. Hu, J. Xue, L. Dong, Y. Jiang, X. Wang, L. Qu and L. Dai, *ACS Nano*, **10**, 1325 (2016).
124. B. Wicklein, A. Kocjan, G. Salazar-Alvarez, F. Carosio, G. Camino, M. Antonietti and L. Bergström, *Nat. Nanotechnol.*, **10**, 277 (2015).

Professor Pil J. Yoo is the professor of School of Chemical Engineering and SKKU Advanced Institute of Nanotechnology (SAINT) at the Sungkyunkwan University (SKKU) of Korea. He received his BS (1998), MS (2000) and PhD (2004) in the department of chemical engineering from the Seoul National University of Korea. He has also worked as a postdoctoral associate in the department of chemical engineering of the Massachusetts Institute of Technology (MIT), then he joined as the faculty of the School of Chemical Engineering of SKKU in 2007. He has published more than 140 SCI papers including Nature Materials, Advanced Materials, Advanced Functional Materials, and ACS Nano, etc. Also, His research works have been cited more than 7,400 times and his H-index is 37. He is serving an associate editor of 'Korean Journal of Chemical Engineering (ISSN: 0256-1115)' and 'NANO (ISSN: 1793-2920)'. Currently, his research expertise includes interfacial manipulation of functionalized thin films using multiscale architecturing methods and organic/inorganic hybridization for next-generation energy device and environmental applications.